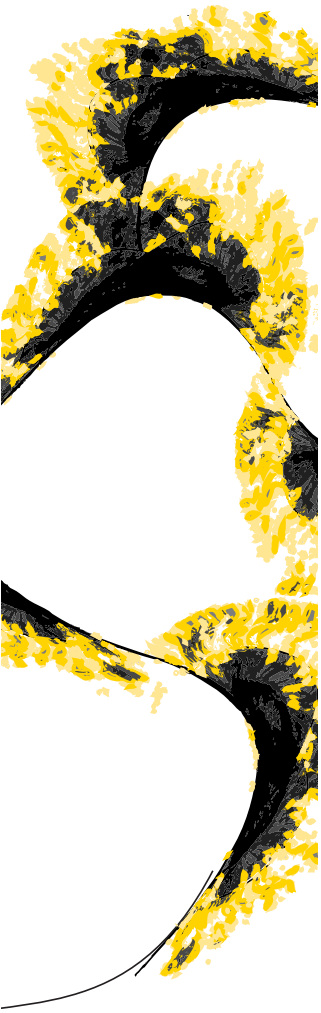

RAM ROBOTICS AND MECHATRONICS

QUALITATIVE FLOW SENSING WITH 3D-PRINTED SENSORS FOR APPLICATION IN A ROBOTIC BIRD

R. (Rutger) van den Berg

BSC ASSIGNMENT

Committee:
prof. dr. ir. G.J.M. Krijnen
ir. A.P. Dijkshoorn
ir. L.H. Groot Koerkamp
dr. A. Sadeghi

June, 2021

045RaM2021
Robotics and Mechatronics
EEMathCS
University of Twente
P.O. Box 217
7500 AE Enschede
The Netherlands

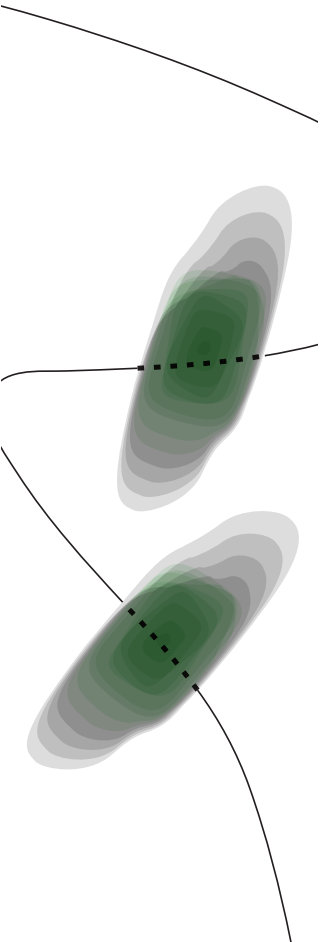

UNIVERSITY OF TWENTE. | TECHMED CENTRE UNIVERSITY OF TWENTE. | DIGITAL SOCIETY INSTITUTE

Summary

Robotic birds are a promising technology for a variety of purposes regarding bird control and to increase knowledge about bird flight. Currently robotic birds are not very autonomous yet. That is why more insight is required in flapping flight.

This report is about the design, fabrication, characterisation and testing of a 3D-printed sensor for qualitative measurement of stall over an airfoil. For this, the concept of the tuft is combined with that of a piezoresistive strain gauge to make a flexible sensor of which the resistance changes as a result of the deflection.

On a aeroelastical level the tuft shows clear flapping behaviour when the airfoil on which it is mounted is under stall. At laminar flow the sensor does not move. High speed video analysis is used to investigate this behaviour.

The resistance of the strain gauge shows fluctuations when the sensor is deflected by an initial force and then released. These fluctuations are in agreement with the flapping of the tuft. A decrease in average resistance is measured as a result of this flapping. However, when tested in the wind tunnel no fluctuations are measured in the resistance due to unknown effects that occur because of the presence of the wind.

Acknowledgements

The past ten weeks have been dedicated to my bachelor's assignment for the bachelor Advanced Technology. I am happy to say that this report is finished and that I am satisfied with the result. But I could not have done this without the help of many people, of which I would like to thank some here:

I would like to thank Alexander Dijkshoorn for his guidance and ideas, for keeping me sharp, helping me out in the lab and giving useful feedback on my report.
I would like to thank Luuk Groot Koerkamp, for his assistance on the aerodynamical part and help in the wind tunnel lab and with the camera measurements.
I would like to thank Gijs Krijnen, for wanting to be the chair of my BSc assignment committee, for his input during our biweekly meetings and his feedback on my progression.
I would like to thank Ali Sadeghi, for willing to be the external member of my BSc assignment committee.
I would like to thank Martijn Schouten, for helping me out with the 3D-printer and giving me useful advise on the printing settings.

Lastly, I want to thank my family and friends for supporting me and being there for me. Thanks to you I have stayed enthusiast and motivated.

Rutger van den Berg
Enschede, 25 June 2021

Contents

1 Introduction

1.1 Problem statement

In the past few years, the company Clear Flight Solutions B.V. [1] has developed the Robird, in collaboration with the University of Twente. The Robird is a robotic bird mimicking a peregrine falcon in appearance, weight, size and flying speed [2]. On top of this, it is a flapping-wing aerial vehicle, making it very difficult for birds to distinguish the Robird from a real falcon. Robotic birds like these can be used for a variety of purposes, such as bird control, e.g. keeping airports free of birds.

Despite it being a very interesting and promising device, much is still unknown about the way the Robird flies. It is designed for simplicity for the operator: currently it is controlled manually, like an RC plane. On top of that, it can only flap in steady-flight with symmetric flapping. To improve its resemblance with real birds, make it fly more energy-efficient and ultimately enable it to take-off, land and make complex maneuvers by itself, more insight is required in the wing-air interaction. The Portwings Project [3] continues developing the Robird, in order to use it as a tool to study bird flight, a topic that is yet unsatisfactorily understood.

The twofold goal of the research on the Robird is thus to increase the autonomy of the Robird and the knowledge about flapping-flight. For this project, the focus lies on developing a sensor to measure airflow over the wings of the Robird. This sensor will be able to be mounted on different locations on the wings of the Robird to measure (dynamic) stall over the wings.

1.2 Related work

Research has shown that flapping wings can induce leading-edge vortices [4, 5] (see figure 1.1), due to viscous effects. Because of this, dynamic stall occurs, which is used by birds to generate more lift.

To take a first step in the direction of measuring such flow properties at the wings of the Robird, a flow sensor [6] has been developed using 3D-printing, at the Robotics and Mechatronics (RaM) research group at the University of Twente. This sensor can be seen in figure 1.2 and was designed to measure the free stream velocity in a quantitative way. It consist of a stiff plate on a flexible section with strain gauges, that deforms due to the drag forces.

The development of this flow sensor shows that it is possible to fabricate a flow-sensing sensor using conductive materials in a 3D-printer. More research [7] is done at the RaM group, into the fabrication process of such sensors. It is shown that 3D-printing is already used in various disciplines to manufacture sensors in a cheap and simple way. On top of that, it offers the possibility to make embedded sensors.

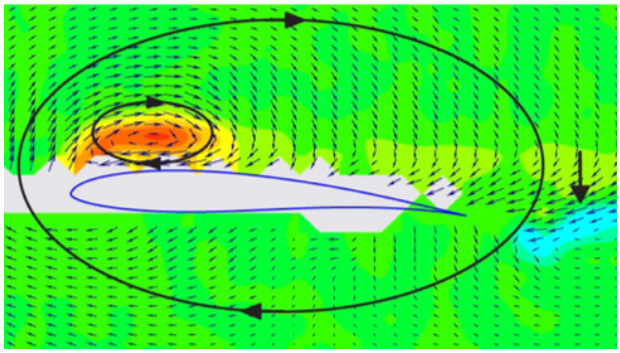

Figure 1.1: Vector field of the flow velocity on top of an airfoil, after subtraction of the average velocity and vorticity field, at a static angle of attack of 4°. The leading edge vortex can be seen in the orange-colored part. [5]

Figure 1.2: A 3D-printed sensor with piezo-resistive strain gauges for quantitative flow sensing, developed at the RaM group [6]

However, noise and non-linearities such as hysteresis and creep in the signals from the sensor in figure 1.2 made it difficult to do quantitative measurements with it. On top of that, such a sensor is too big and heavy to put on the wings of the Robird and will induce a large amount of additional drag. The demand came for a sensor that would be able to measure the presence of (dynamic) stall on a wing, without heavily distorting the flow. It was decided to make a sensor that can just produce qualitative information. Birds, when flying, do not know their exact speed or angle of attack, they can simply sense if they are flying correctly, so a qualitative measurement would have to be sufficient. This would circumnavigate problems with non-linearities as well, giving the possibility for simpler measurements.

1.3 Research goal

This project will build further on the developments mentioned in the previous section. It is about the design, fabrication and characterisation of a sensor for measuring stall over an airfoil. The research question that will be central in this report is:

To what extend is it possible to use the principle of a piezoresistive strain gauge in a 3D-printed sensor to measure the presence of stall over an airfoil in a qualitative way?

There are a few important challenges that need to be dealt with. The first problem to face will be the fact that it is not clear yet, how to actually measure the presence of stall. Other challenges are the accuracy of the 3D-printing, the sensitivity of the sensor, the effect of the movement of the wings and the effect of the sensor itself on the flow. The sensor must be sufficiently small, such that multiple sensors can be placed on different locations on the wing, to gain distributed flow information. These points of attention must all be kept in mind into account when designing this sensor.

1.4 Overview of report

First of all, research will be done to define the theoretical background and possible concepts of this sensor, on which will be elaborated in chapter 2. Next, requirements for the sensor will be mentioned and the sensor will be designed, which is in chapter 3. In chapter 4 the fabrication process will be explained. Then, chapter 5 will describe the measurement set-up and methods used to gather data on the sensor and its behaviour. The results of these test will then be showed in chapter 6. Lastly, chapter 7 will discuss on these results and a final conclusion will be drawn in chapter 8.

2 Theoretical background

2.1 Introduction

In this chapter, an overview of the theoretical background required to understand the problem defined, is given. First, both static stall and dynamic stall are looked into. After that, the fluid-solid interaction is treated at a conceptual level. Lastly, the principle of the strain gauge is elaborated on.

2.2 Wing aerodynamics

2.2.1 Steady wing

Although a flapping wing situation is what the sensor eventually could be applied to, measuring with a sensor on a flapping wing is way more complicated. On top of that, a fully working flapping-wing setup was not available to test the sensor on at the start of this project. It was therefore decided to design and test the sensor on a steady airfoil.

To understand the concept of stall, it is useful to first look at the way an airfoil generates lift. When air flows over an airfoil, the air that flows over the wing has to travel a longer way than the air that goes underneath it, due to the characteristic shape of airfoils. The Kutta Condition [8] states that the two flows have to 'line up' again at the trailing edge. This causes the air above the wing to move faster. The Bernoulli Equation [8] then states that this faster moving air has a lower pressure. In figure 2.1 (attached flow), the pressure distribution for such a case can be seen. The air pressure under the wing is higher than above the wing, resulting in an upward force called lift.

It can be seen in the figure as well, that the pressure is small at the leading edge and larger at the trailing edge. Thus, the air flows from low to high pressure, which is contradicting to a fundamental concept of fluid, namely that it flows from high to low pressure. Viscous effects in the boundary layer make sure that the air flows from low to high pressure anyway. However, when the angle of attack (AOA) is increased, these viscous effects will eventually no longer be strong enough to keep the flow attached. The flow will then separate and vortices will be formed, moving the air again from the high-pressure trailing edge towards the low-pressure leading edge. This can be seen in figure 2.2. When this occurs, the pressure differences over the chord length will decrease and a rapid decrease of lift will be the result, as can be seen in figure 2.1 (separated flow). This is called stall.

2.2.2 Flapping wing

As has already been discussed in chapter 1, a very important concept in flapping wing aerodynamics is the leading edge vortex (LEV). When an airfoil is suddenly accelerated to a certain velocity, it can take up to 6 chord lengths of travel until the lift has reached 90 percent of the steady-state values [4], which can be explained by the Wagner effect [10, 11]. However,

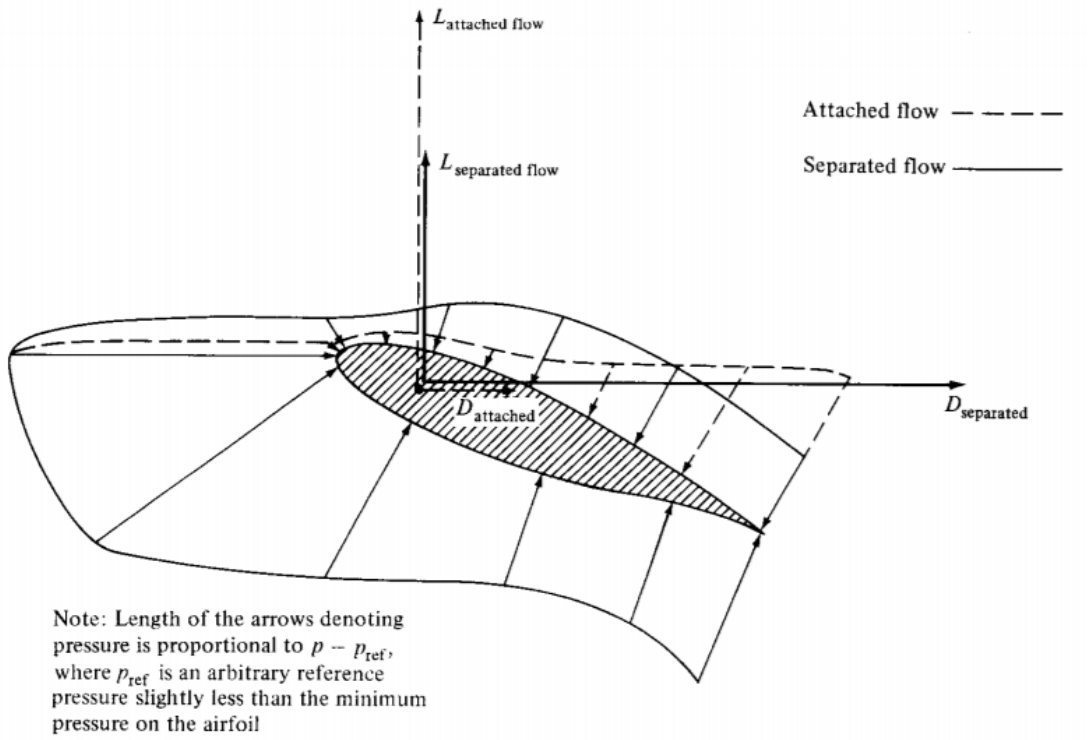

Figure 2.1: The pressure distribution at an airfoil under a large AOA, for both attached and separated flow [9]

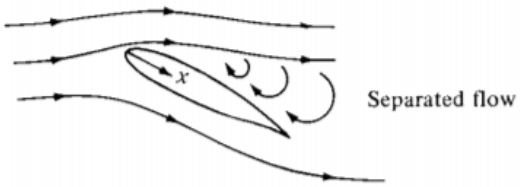

Figure 2.2: Streamlines of separated flow [9]

when this sudden acceleration is done at an AOA above the dynamic stalling angle, a large vortex is created [12]. This LEV starts at the leading edge and, depending on the wing speed and chord length of the wing, rolls over towards the trailing edge, creating flow reversal at the surface of the wing. A visualisation of leading edge vortices using colour coding can be found via https://vimeo.com/141632065 [13]. In figure 1.1, a vector field of the flow velocity can be found.

During this process, an additional lift component is generated during downstroke [14]. The amount of this additional lift is among others dependant on the flapping frequency,

making it relevant to know when this effect occurs. However, as has been explained, static stall is what this research focuses on. The difference here is that dynamic stall primarily occurs on the leading edge, whereas the vortices in static stall are primarily found on the trailing edge.

2.3 Fluid-solid interaction

Now that the aerodynamics have been introduced, it is necessary to look at the interaction between the air and the sensor, to understand what behaviour of the sensor can be expected. In this interaction between fluid (air) and solid (sensor) many factors are present. It is difficult to describe and predict them, due to the fact that the flow properties influence the movement of the sensor, and the sensor itself has an influence on the flow around it. On top of that, the sensor will move partly within and partly out of the boundary layer. Since there is a lot of unpredictable behaviour occurring at stall, it is hardly possible to analytically model the dynamic movement of the sensor.

However, it is possible to scale the problem and find dimensionless parameters that describe the relation between fluid and solid. That is what this section is about. This derivation is based on the course 'Fundamentals of fluid-solid interactions' by Coursera [15].

First, in table 2.1, an overview is given of all parameters that are present in a general fluid-solid interaction case.

fluid			**solid**
coordinates	$\vec{x}$	$\vec{x}$	coordinates
time	t	t	time
velocity field	$\vec{U}$	$\vec{\xi}$	displacement field
viscosity	μ	E	stiffness
size	L	L	size
gravity	g	g	gravity
density	ρ_f	ρ_s	density
velocity data	U_∞	ξ_0	displacement data

Table 2.1: Overview of parameters present in fluid and solid domain

Assume that there is a function f relating all the parameters in the fluid domain:

$$f(\vec{x}, t, \vec{U}, \mu, L, g, \rho_\mathrm{f}, U_\infty) = 0 \tag{2.1}$$

In this function, 8 parameters and 3 fundamental dimensions (length, mass and time) are present. The Buckingham Pi theorem [8] can be used to come up with 5 dimensionless parameters, which will give the dimensionless function F:

$$F\left(\frac{\vec{U}}{U_\infty}, \frac{\vec{x}}{L}, \frac{U_\infty t}{L}, \frac{\rho_\mathrm{f} U_\infty L}{\mu}, \frac{U_\infty}{\sqrt{gL}}\right) = 0 \tag{2.2}$$

The same can be done for the solid domain. A function is defined that relates all the parameters in the solid domain:

$$g(\vec{x}, t, \vec{\xi}, E, L, g, \rho_s, \xi_0) = 0 \tag{2.3}$$

Again, 8 parameters and 3 fundamental dimensions are present, so 5 dimensionless parameters are identified and a dimensionless function is found:

$$G\left(\frac{\vec{\xi}}{L}, \frac{\vec{x}}{L}, \frac{t\sqrt{E/\rho_s}}{L}, \frac{\xi_0}{L}, \frac{\rho_s g L}{E}\right) = 0 \tag{2.4}$$

Now, these two systems can be coupled. A function h is defined that relates all the present parameters, which are 11. There are still 3 fundamental dimensions, so 8 dimensionless parameters need to be defined. For this, all 5 dimensionless numbers of the fluid and the last 2 of the solid are used. The 8th parameter, which will now be called X, has to be a combination of fluid and solid.

$$h(\vec{U}, \vec{x}, t, \mu, \rho_f, \vec{\xi}, E, L, g, \rho_s, \xi_0) = 0 \tag{2.5}$$

$$H\left(\frac{\vec{U}}{U_\infty}, \frac{\vec{x}}{L}, \frac{U_\infty t}{L}, \frac{\rho_f U_\infty L}{\mu}, \frac{U_\infty}{\sqrt{gL}}, \frac{\xi_0}{L}, \frac{\rho_s g L}{E}, X\right) = 0 \tag{2.6}$$

In this equation, a few well-known parameters are identified, such as the Reynolds number Re, the Froude number Fr and the displacement number D:

$$Re = \frac{\rho_f U_\infty L}{\mu} \tag{2.7}$$

$$Fr = \frac{U_\infty}{\sqrt{gL}} \tag{2.8}$$

$$D = \frac{\xi_0}{L} \tag{2.9}$$

There are a few possible options for the yet unknown parameter X. The first option is the mass ratio M, which gives a measure for the effect of the added mass and is defined as the ratio between the densities of fluid and solid. When using air as a fluid, the mass ratio will be low (about 0.001), since the density of solids is generally about 1000 times higher than that of air.

$$M = \frac{\rho_f}{\rho_s} \tag{2.10}$$

Another option would be the reduced velocity U_r, which is defined as the flow velocity divided by the scale of elastic waves in the solid. The closer this value is to 1, the more interaction is expected.

$$U_r = \frac{U_\infty}{\sqrt{E/\rho_s}} \tag{2.11}$$

The last option is the Cauchy number Ca, which is the ratio between the dynamic pressure in the fluid and elasticity modulus in the solid. The higher this value is, the more the solid deforms under the pressures in the fluid [4].

$$Ca = \frac{\rho_f U_\infty^2}{E} \tag{2.12}$$

These last three dimensionless numbers are the most interesting ones, since these describe the relation between fluid and solid, whereas the 7 parameters in equation 2.6 describe either fluid or solid properties. When the sensor is designed, the mass number, reduced velocity and Cauchy number will be looked into in more detail. This can be found in section 3.6.3.

2.4 Strain gauge

Since the aim of this project is to develop a 3D-printed sensor, a limited number of possibilities is available to design a way to measure displacements of, or forces on, the sensor. One way, on which a lot of research has been done at the RaM group [7,16], is using the piezoresistive effect, which states that the electrical resistivity of a conductive material changes when mechanical strain is incurred, on which will be further elaborated in section 3.6.2. This effect can be applied to make a so-called strain gauge.

A strain gauge in its simplest form consist of two parts: an insulating substrate and a conductive film, which is oriented in the direction in which the strain will act. An example can be seen in figure 2.3. Such a strain gauge can be easily fabricated using fused deposition modelling (FDM) [17] 3D-printing, since this gives the opportunity to print the conductive film on top of the substrate. The next chapter will discuss the sensor concepts on which such a strain gauge could be applied.

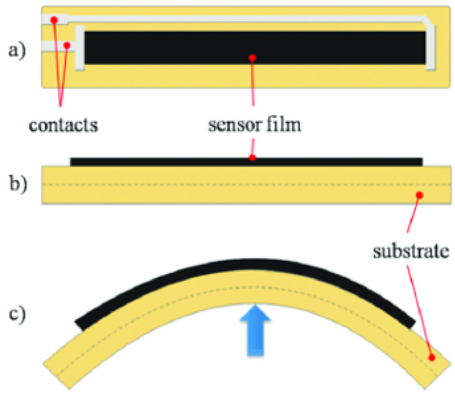

Figure 2.3: A strain gauge seen from the top (a) and side (b) in the default state and from the side in a displaced state (c) [18]

2.5 Conclusion

In this chapter, a qualitative framework is set up for the sensor. The basic aerodynamics for both the static and dynamic case are introduced, as well as the fluid-solid interaction. The Mass ratio, reduced velocity and Cauchy number are found as dimensionless numbers that may be used to describe this fluid-solid interaction. The principle of the strain gauge is explained, which will be used as a way of measuring strain in the sensor. The next chapter will show a few concepts to which this principle can be applied.

3 Design

3.1 Introduction

In the previous section, a qualitative framework was set up. Now, a few objectives will be defined for the sensor. A few possible concepts will then be discussed, after which one of these concepts is used to further explore and develop the sensor. After that, the further design process will be described and a few characteristics of this sensor will be analytically determined, which are to be tested later on.

3.2 Objectives for the sensor

In this list, the major objectives for the sensor are summarized. These objectives are based on an evaluation of the knowledge gathered in chapter 2 and the goal for this project as defined in chapter 1, namely to research the possibilities for developing a sensor to measure the presence of stall over an airfoil in a *qualitative* way.

1. The sensor must be able to measure stall in a qualitative way;
2. The sensor must disturb the flow as little as possible, such that no large increment in drag forces is induced;
3. The sensor must be small, compared to the size of the wing of the Robird, such that multiple sensors can be placed on the wing simultaneously and distributed flow information can be gathered;
4. The sensor must have a low stiffness, since the resistance change will be measurable better if the displacement of the sensor is larger;
5. As little energy as possible should be used to power the sensor, since the Robird has a limited battery capacity;
6. The sensor must be fabricated using FDM 3D-printing.

3.3 Possible sensor concepts

In this section, a few existing sensor concepts are described, which are used to measure flow properties and could be used in combination with a strain gauge for measuring stall over an airfoil.

3.3.1 Hair-inspired sensors

Hairs are found a lot in nature, and are used by all different kinds of animals as flow or tactile sensors. The concept could be used to make a cylindrical or rectangular hair, with a strain gauge on one side. This hair will be placed perpendicular to the flow direction. At normal flow, the sensor will bend towards the trailing edge, but when flow reversal occurs, it will bend over to the other side. This effect should be measurable. Such sensors have already been

made to measure the difference between laminar and turbulent flow quantitatively [19]. A study into the effect of different parameters for the design of such a hair-inspired flow sensor can be found in [20].

A big advantage of this sensor is its small size, because of which many sensors can be placed on the wing to get distributed flow information. This can be used to get accurate information on the location of flow separation [21].

However, there might be a reason why birds are generally not the animals on which hairs can be found. A hair, standing perpendicular to the flow, will induce a large amount of drag, which is disadvantageous for the flying efficiency of the bird. On top of that, it is hardly possible to 3D-print such a sensor, as the strain gauge will be perpendicular to the layer direction in which is printed. This will not be beneficial for the quality of the print. It could be possible to print the sensor on its side, to avoid this problem, but then it is more difficult to print a cylindrical sensor. It then has to be made rectangular, increasing drag even more, since a rectangular hair will have a higher drag component than a cylindrical one with the same diameter [8].

3.3.2 Tuft

As said, birds do not have hairs to measure flow, but rather use feathers. The advantage of feathers is the fact that they their steady state is not perpendicular, but parallel to the flow, which greatly reduces the extra amount of drag. This same advantage can be found in the tuft. Although little literature is available about them, tufts have been used in airplane design for a long time [22]. In its most simple form, a tuft is a piece of rope, taped on top of an wing at its base. Due to its very low stiffness, it will move with the flow very easily. When the flow is laminar, the tuft will just lie on the airfoil and not move, but as soon as vortices are present, it will start flapping. At flow reversal, it will reverse with the flow.

Generally, when tufts are applied, they are covered with a luminescent paint, to be able to visually detect them [23, 24]. For a robotic bird flying high in the sky, this is of course not practical. However, again the principle of the strain gauge could be applied, by designing the sensor as a very slender strain gauge. The movement of the sensor, whether it is flapping, swishing or reversion, can be denoted by resistance changes.

As can be seen in a visualisation [25], the movement of the tuft will be very unpredictable once stall occurs, making it very hard to model. This will be a disadvantage of this concept. However, for qualitative measurements this is not a big problem.

3.3.3 Stall flag

In his PhD thesis [26], Gustave Paul Corten has described his research into using so-called stall flags for visualisation of flow separation on a wind turbine. A stall flag consists of a flap on a hinge, which can be in two positions, depending on the direction of the flow. It has a small opening angle, because of which there is a small volume of air below the flap. As the

flow reverses, there will be a large pressure increase in this volume, which makes the flap move to its other state. A schematic visualisation can be seen in figure 3.1. In this specific case, it is used with a reflective surface with is covered in one state but open in the other.

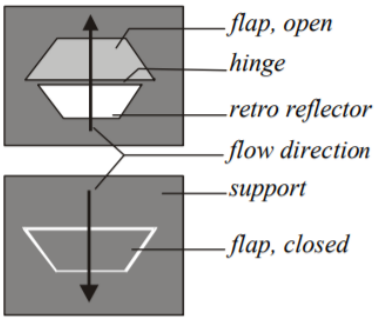

(a) A stall flag in its two extreme states [26]

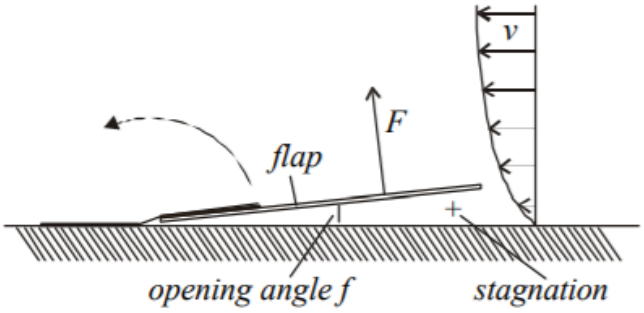

(b) The switching stall flag [26]

Figure 3.1: A schematic view of the stall flag [26]

This principle could be used on a bird wing as well, by designing it in such a way that an electric signal is sent once the stall flag reaches the other state. Due to its design, the stall flag will always be in one of two states and not in a different position in between, making it good for qualitative measurements. Another advantage is that the influence on the flow will be little, since it only moves when the flow switches states. However, the design of the stall flag is more complex than that of the hair or tuft, e.g. due to the fact that it has a hinge structure. On top of that, in a structure like this, it is more difficult to apply the principle of the strain gauge, as there is no deformation in the sensor. Another way should be developed to measure the state of the sensor.

3.4 Concept decision

Taking the formulated objectives in consideration, a decision will now be made on the concept to continue the design phase with. First, the advantages and disadvantages of the concepts are briefly summed up in table 3.1.

	Advantages	Disadvantages
Hair-inspired	Small	High induced drag Difficult to 3D print using FDM
Tuft	Low induced drag Easy to fabricate	Unpredictable behaviour
Stall flag	Qualitative measurements Low induced drag	More complex to fabricate No strain gauge possible

Table 3.1: Advantages and disadvantages of the different design concepts

The concept of the hair-inspired sensor will not be used, since such a hair will induce a large drag component. Combined with the fact that it is hard to print such a sensor with FDM, it is decided not to continue with this design concept.

The stall flag is considered a viable option, since it is designed to measure in a qualitative way and has little influence on the flow. However, it more complex design makes it not the best option for this project.

Due to its straightforward design, its very small size and its minimal influence on the flow, it it decided to continue the design phase with the tuft. A disadvantage will be the unpredictability of the exact movement of the sensor, but this is not a big problem, since the measurements will be qualitative only.

The design of the sensor will thus consist of a tuft with a strain gauge on top of it as shown in figure 3.2. To keep the stiffness as low as possible, the cross-sectional area of the sensor will have to be made as small as possible, a few mm^2 at most. The length will be in the order of centimeters, to make the tuft very slender. There are a few restrictions on the design due to the properties of the 3D-printer, which will have an effect on the final design.

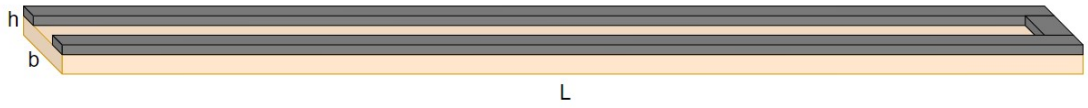

Figure 3.2: Conceptual design: a tuft (orange) with a strain gauge (black) on top of it

3.5 Detailed design

As will be discussed further in chapter 4, the mean traxel width is 0.4 mm and the layer height is 0.1 mm. These sizes are taken as starting point for the detailed design, as it is of course necessary to print an exact number of lines and layers. The design discussed in this section is the final design. A few specific changes in the design, that had to be made during the printing process, will be briefly explained in section 4.2.4.

3.5.1 Cross-section

To make sure the stiffness of the sensor is small enough, the cross-sectional area should be as small as possible. It consists of only two layers: The first layer with the base material, on which the strain gauge is printed in a second layer. The strain gauge goes from the base to the end of the sensor and back, giving it an effective length of twice the sensor length. The width of the strain gauge will be one line only, i.e. 0.4 mm.

3.5.2 Length

The length of the sensor is expected to have a large influence on its mechanical behaviour. The longer and more slender the sensor, the easier it will lash out as a result of the aerody-

namical forces. Therefore, it is decided to design sensors with different lengths, to investigate the effect of this. Lengths of 20, 30, 40, 50 and 75 mm are chosen. This will give a range of lengths from a small to a large fraction of the Robird's wing chord length.

3.5.3 Final design

The sensor needs wiring to a device to measure its resistance. Therefore, a base of 5 by 10 mm is added to the sensor, on which two contact pads are printed, which are connected to the two sensor legs. With this, the design is completed. An image of the final design can be seen in figure 3.3. Here, the sensor with a length of 30 mmis taken as an example. The other sensors are identical, but with different lengths.

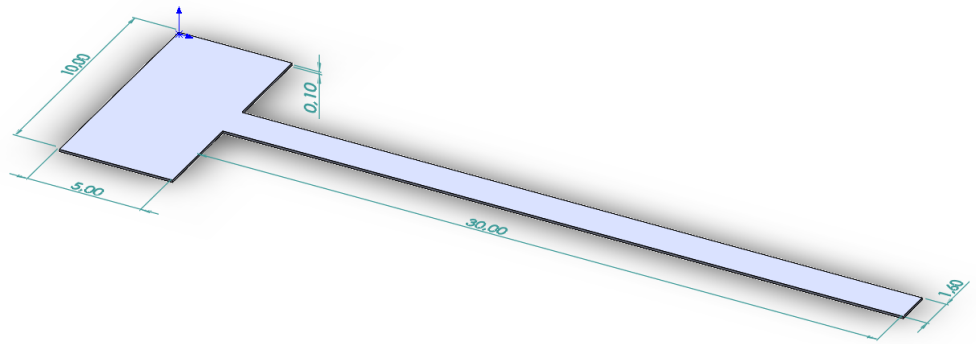

(a) The base of the sensor

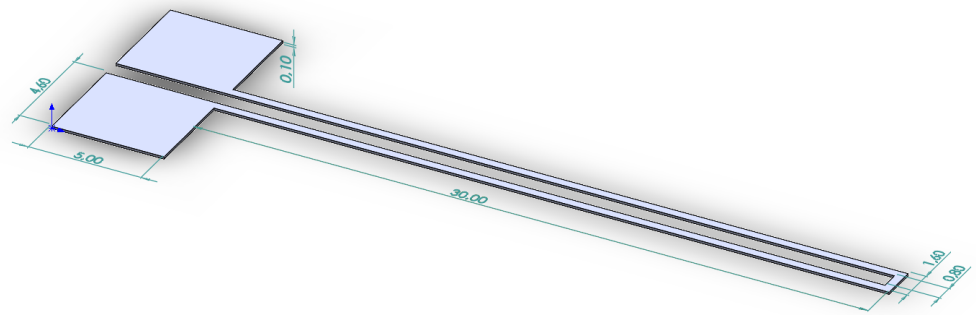

(b) The strain gauge of the sensor

Figure 3.3: The final design of the sensor, as designed in Solidworks 2020 (dimensions in mm)

3.6 Analytically determined characteristics

Now that the design of the sensor is completed, a few characteristics can be analytically determined. These characteristics will give some useful information on the effect of the length on the sensor. When doing measurements, these will be evaluated.

3.6.1 Cantilever beam assumption

When considering the tuft as a rectangular cantilever beam, the stiffness is an important variable. Because multiple stiffnesses can be defined for a beam, specifically the flexural rigidity will be looked into. The flexural rigidity is the product of the Elasticity Modulus (E) and the second moment of area in the bending direction (I_y). E is given to be 12 MPa for both materials the sensors are printed with, as will be shown in chapter 4. I_y can be calculated by the following equation:

$$I_y = \int_{A_c} y^2 dS = \int_{-\frac{b}{2}}^{\frac{b}{2}} \int_{-\frac{h}{2}}^{\frac{h}{2}} y^2 dy dx = \frac{bh^3}{12} = 1.0667 \cdot 10^{-15}\ \mathrm{m}^4 \tag{3.1}$$

Here, b is the width and h the height of the sensor. The y-direction is the vertical direction, i.e. the bending direction of the sensor. The cross-section lies in the xy-plane, the length of the tuft is in the z-direction.

The flexural rigidity of the beam is now calculated to be $1.28 \cdot 10^{-8}$ N m^2. This is very low, because of which it is assumed that the tuft will not behave as a cantilever beam. This hypothesis will be tested later on. If it would be possible to consider the tuft to be a cantilever beam, the first eigenfrequency would be given by [27]:

$$\omega_n = 1.875^2 \sqrt{\frac{EI_y}{\rho_s A_c L^4}} \tag{3.2}$$

The calculated eigenfrequencies can be found in table 3.2.

Length (mm)	20	30	40	50	75
First eigenfrequency (Hz)	50.5	22.5	12.6	8.1	3.6

Table 3.2: The eigenfrequency for different lengths

3.6.2 Resistance

The resistance of the strain gauge in horizontal shape can be calculated with the following equation, where the factor 2 comes from the fact that the effective length of the strain gauge is equal to twice the length of the sensor:

$$R_0 = \frac{2\rho L_0}{A_s} \tag{3.3}$$

Here, A_s is the cross-sectional area of the strain gauge. It is assumed that the centerline of the bending of the sensor lies exactly in the middle. In reality, it will lie slightly below this, because the strain gauge does not cover the entire area of the base. The center of the strain gauge lies a small distance higher than the centerline of the bending of the sensor, which will furthermore be denoted by e. In this design, $e = 0.5$ mm (half a layer thickness). This will cause a slight elongation or compression of the strain gauge when the sensor is bent. For this analysis, it is assumed that the sensor only bends upwards and will have the shape of an arc, as can be seen in figure 3.4.

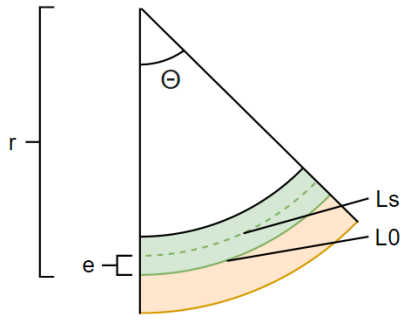

Figure 3.4: A schematic side view of the bent sensor. The base is shown in orange, the strain gauge in green. Lengths L_0 and L_s are indicated, as well as e, r and Θ

It is furthermore assumed that the strain is constant over the thickness of the strain gauge, which is only valid for small deflections due to the relative large thickness of the strain gauge, with respect to the thickness of the tuft. The relation between the bending angle in radians Θ, bending radius r and length of sensor L_0 is given as:

$$r = \frac{L_0}{\Theta} \tag{3.4}$$

The bending radius of the center of the strain gauge is now given as $r - e$, as a result of which the length of the center of the strain gauge $L_s = \Theta(r - e)$. The definition of r can be used to rewrite this as:

$$L_s = L_0 - e\Theta \tag{3.5}$$

The strain ϵ of the strain gauge is then given by:

$$\epsilon = \frac{\Delta L}{L_0} = \frac{L_s - L_0}{L_0} = \frac{-e\Theta}{L_0} \tag{3.6}$$

To calculate the change in resistance due to this strain, the gauge factor (GF) is required. The gauge factor is the ratio of relative change in electrical resistance, to the mechanical strain and is given by: [28]

$$GF = 1 + 2\nu + \frac{\frac{\Delta\rho}{\rho}}{\epsilon} = \frac{\frac{\Delta R}{R_0}}{\epsilon} \tag{3.7}$$

Here, ν is the poisson ratio, which has a value of around 0.5 for TPU [29]. The GF for ETPU has a value of 20 [30]. It is now possible to describe the relative change in resistance as a function of Θ and L_0, by combining equations 3.6 and 3.7:

$$\frac{\Delta R}{R_0} = \frac{-e\Theta}{L_0} \cdot GF \tag{3.8}$$

In figure 3.5, this relative resistance decrease is plotted as function of the bending angle, for the 5 different lengths of the sensor. It can be seen that this difference will be 16 % at most, and will be larger for shorter sensors.

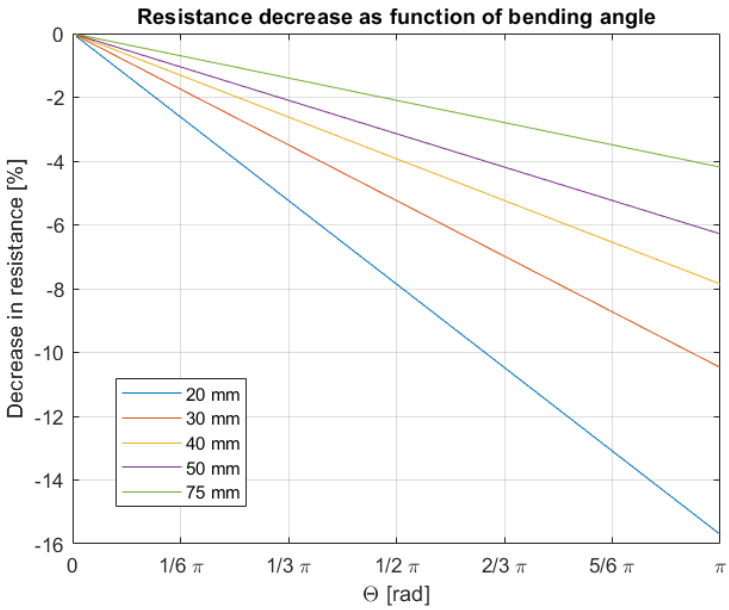

Figure 3.5: Resistance change as function of bending angle

3.6.3 Dimensionless numbers

In section 2.3, dimensionless numbers are introduced to describe the interaction between fluid and solid. Three possible numbers are defined: the mass number, the reduced velocity and the Cauchy number. The mass number has a value of 0.001 in this situation. This indicates that the inertia of the air that needs to be displaced due to the displacement of the sensor (the added mass) is negligible. The reduced velocity, for the given parameters, equals 0.1004. This value is an order of magnitude away from 1, meaning that there will be no direct coupling. However, there will still be some interaction.

These values for the mass number and the reduced velocity are constant for all lengths of sensors. However, to investigate the effect of the length of the sensor, a parameter must be found that contains parameters from both the fluid and solid domain, and has the length L in it. This is where the Cauchy number comes in. Although equation 2.12 does not have L in it, it is possible to define a more accurate Cauchy number, which is a function of the length. This will now be discussed.

In section 2.3, the Cauchy number was defined as the ratio between the dynamic pressure in the fluid and elasticity modulus in the solid. As said, the definition as given is not a function of the length of the sensor. When calculated, it has a value in the order of magnitude 10^{-5}. Such a low value would mean that no deformation can be found at all in the sensor, which is obviously incorrect.

For slender elements, a more accurate Cauchy number can be found by taking the so-called

slenderness ratio [31] into account. The slenderness ratio $\mathcal{S}$, defined as the ratio between the length and the radius of gyration, which is a measure of the elastic stability of a cross-section against buckling [32]. The radius of gyration in the y-direction, for a rectangular cross-section, is given by $\sqrt{I_y/A_c}$ [33]. The slenderness ratio is thus given by:

$$\mathcal{S} = \frac{L}{\sqrt{I_y/A_c}} \tag{3.9}$$

The more accurate Cauchy number is then calculated by multiplying equation 2.12 by $\mathcal{S}^3$ [34]:

$$Ca = \frac{\rho_f U_\infty^2}{E} \cdot \mathcal{S}^3 \tag{3.10}$$

With $I_t exty$ calculated in equation 3.1, the slenderness ratio can be calculated and the Cauchy number can thus be determined as a function of the sensor length. In table 3.3, the calculated Cauchy number for different lengths can be found for $U_\infty = 10\,\mathrm{m\,s^{-1}}$.

Length (mm)	20	30	40	50	75
Cauchy number	424.35	1432.2	3394.8	6630.5	22378

Table 3.3: The Cauchy number for different lengths, $U_\infty = 10\,\mathrm{m\,s^{-1}}$

As can be seen, the inclusion of the slenderness ratio increases the Cauchy number by 7 to 9 orders of magnitude. The values are now in the order of magnitude $10^2 - 10^4$, indicating that the sensor will have significant deformation due to the flow. It is expected that not all sensors will behave similarly. The largest sensor has a Cauchy number which is 50 times larger than that of the smallest sensor, indicating that the larger sensors will have more deformation.

3.7 Airfoil design

To do wind tunnel tests with the sensor, a NACA 0012 airfoil has been designed and 3D-printed. This airfoil has a chord length of 11.0 cm and a span of 21.0 cm. It has a tube on the trailing edge, with an inner diameter of 10 mm and an outer diameter of 11 mm, using which it can be connected to the wind tunnel. The airfoil, which can be seen in figure 3.6, is printed with PLA.

The aspect ratio (AR) of a wing is given by the following equation, for which the first equality holds for all wings and the second equality for rectangular wings only, which is the case here.

$$AR = \frac{b^2}{S} = \frac{b}{c} \tag{3.11}$$

Here, b is the wing span, S is the wing area and c is the chord length. With the given dimensions, this yields an AR of 1.9 for this airfoil, which is rather low. Therefore, 3-dimensional effects will play a significant role, resulting in the creation of wingtip vortices. This will exert a force on the sensor, in the direction of the center of the airfoil [8]. A schematic view of this

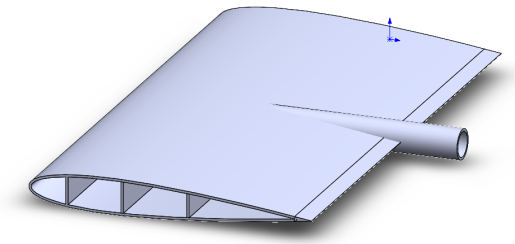

Figure 3.6: The NACA 0012 airfoil, designed in Solidworks 2020, which will be used for wind tunnel measurements with the sensor

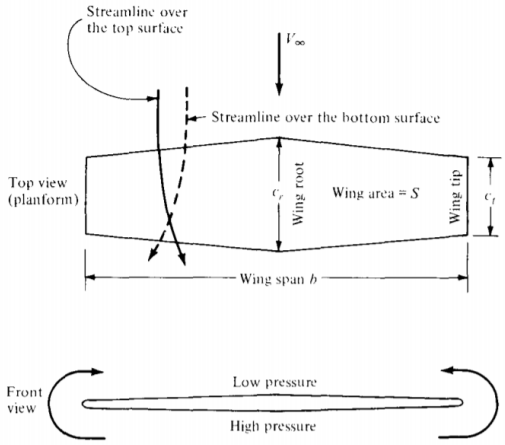

Figure 3.7: Flow over a finite wing [8]

can be seen in figure 3.7. When doing the measurements, it will be checked if this is indeed the case.

Little holes are drilled in the airfoil, at 3.75, 5.5, 7.25 and 9.0 cm from the trailing edge, to put the wires to the sensors through. This way, these wires could go through the inside of the airfoil, rather than over it, which would disturb the flow. The different locations are chosen such that the different lengths can be used on different locations, without having the need to have a long wire over the airfoil.

3.8 Conclusion

After the objectives for the sensor were formulated, a few conceptual designs are evaluated in this chapter. It was decided to continue the design phase with the tuft. After that, a tuft-based sensor with a strain gauge was designed, with different lengths to analyze the effect of this length on the behaviour. For these sensors, the theoretical resistance and the change in this are determined, as well as the Cauchy number. Lastly, an airfoil is designed to do the wind tunnel measurements with. In the next chapter, it will be discussed how this sensor is actually fabricated.

4 Fabrication

4.1 Introduction

This chapter is about the fabrication process of the sensor. After the design was completed, it is drawn in a CAD program, 3D-printed, and post processed to make it into a usable sensor. These steps are described in this chapter.

4.2 3D-printing the tuft

4.2.1 Printer and materials

A Diabase H-series multi-material printer [35] is used for 3D-printing the sensors, as can be seen in figure 4.1a. This printer can print up to 5 different materials in a single print, using FDM. To do so, it uses a rotary toolhead (see figure 4.1b) to change between the materials. The nozzle width is 0.4 mm. The layer thickness is set to 0.1 mm, which is the minimal thickness that can be printed reliably. These properties make this printer very capable of printing this sensor, since multiple materials need to be used and high accuracy is required.

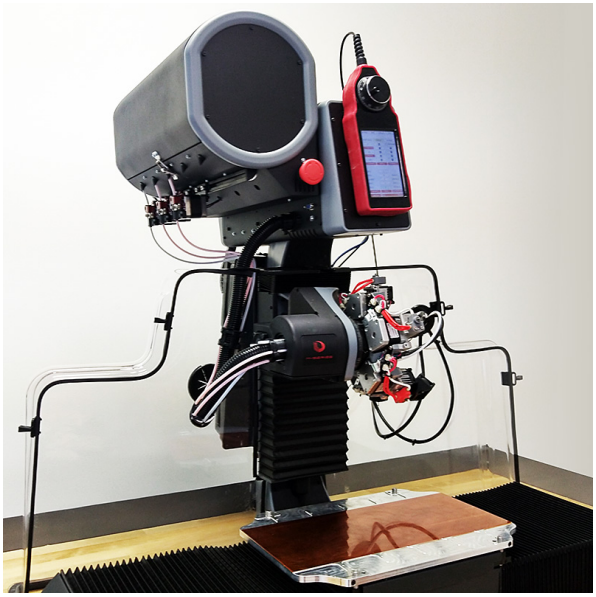

(a) A Diabase H-series 3D-printer [36]

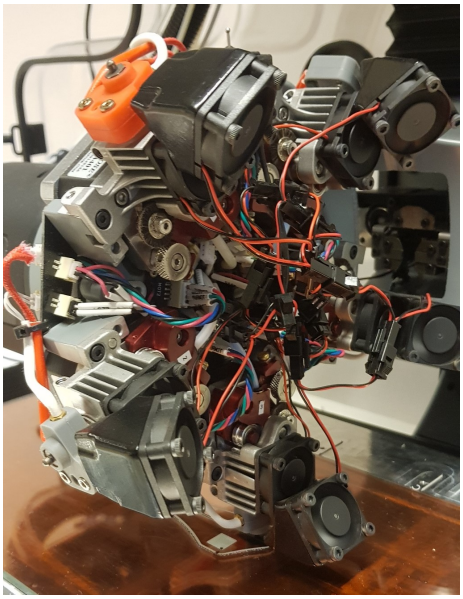

(b) The rotary toolhead of the used 3D-printer

Figure 4.1: The 3D-printer used for 3D-printing the sensors

This printer is provided with a cam dial. This is a dial on the extruder, with which the amount of force on the filament can be varied, to be able to print both soft and stiff materials. The cam dial can be set in a range from 1 (most force) to 4 (least force).

For the base material, Ninjaflex TPU [37] from Ninjatek is used. For the strain gauge material, PI-ETPU 85-700+ [38] of the company Palmiga Innovation is used, which is a conductive ($\rho < 300\,\Omega\,\mathrm{m}$) filament. Both these materials are flexible and have an Elasticity Modulus of 12 MPa.

4.2.2 Drawing and slicing the design

The design of the sensor is drawn in Solidworks 2020 [39]. Here, the base and the strain gauge are designed as two different objects, to make the printing process later on more straightforward, since these two objects need to be printed in different materials. After that, this drawing is made into a 3D-printable object using a slicer. Ultimaker Cura [40] is used for this.

4.2.3 Printing settings

The specific printing parameters such as the filament flow rate are determined empirically by tuning them until the desired quality was been reached. This was an iterative process, of which the shown sensors are the final product. The final values for these settings can be found in table 4.1.

	Base	Strain gauge
Material	Ninjaflex TPU	PI-ETPU 85-700
Printing speed	$15\,\mathrm{mm\,s^{-1}}$	$15\,\mathrm{mm\,s^{-1}}$
Flow rate	150 %	110 %
Printing temperture	228 °C	228 °C
Wall thickness	0.8 mm	0.4 mm
Infill density	100 %	100 %
Cam dial	2	3

Table 4.1: Printing settings

The bed temperature used is 60 °C. Also, a layer of Kapton tape [41] is put over the bed, to make sure the filament is well attached to it. Custom prime towers are added to ensure a smooth flow of the filament. Skirts were used as build plate adhesion type. Since only a few layers are used, both top and bottom layers are disabled, such that all layers have the same printing properties.

The infill is printed before the walls. On top of that, an infill wipe distance of 0.1 mm is set, which means there is a very small overlap between the walls and the infill. These two measures made sure that the infill sticked to the wall better. The wall thickness is set to 0.8 mm, or two lines, for the base, but to only 0.4 mm, or one line, for the strain gauge. This is necessary, since the strain gauge has to be one line only.

4.2.4 Design variations

There are a few specifications in the design that changed during the printing process, on which will be shortly elaborated here.

Initially, the sensor was designed to have a base, with two layers of strain gauge on top of it. In between the two 'legs' of the sensor, one line of substrate material was to be printed, to prevent the strain gauge from making a short circuit. However, during the printing process, it was found that this line of substrate and the second layer of strain gauge caused a lot of smearing, due to the fact that the materials had to be printed after each other, per layer. Due to the fact that the sizes of the sensor are very small, high precision is required to guarantee the quality of the sensor. It was therefore decided to omit the second layer of strain gauge.

Due to unchangeable printer properties, it is required that every part to be printed has to have either at least an inner and an outer boundary, or a fully enclosed boundary with infill, because of which the printer printed the line of strain gauge in two parts. This caused the width of this line to be larger than 0.4 mm, which in turn caused short circuiting some times. To prevent that, the width of the sensor was increased with an extra 0.4 mm, to give more space between the two legs of the strain gauge. The base material in between was no longer needed and therefore left out.

4.2.5 Final prints

In figure 4.2, the printer can be seen in the process of printing a sensor. The orange tape that can be seen on the bed, is the Kapton tape. The white and black squares are the custom prime towers.

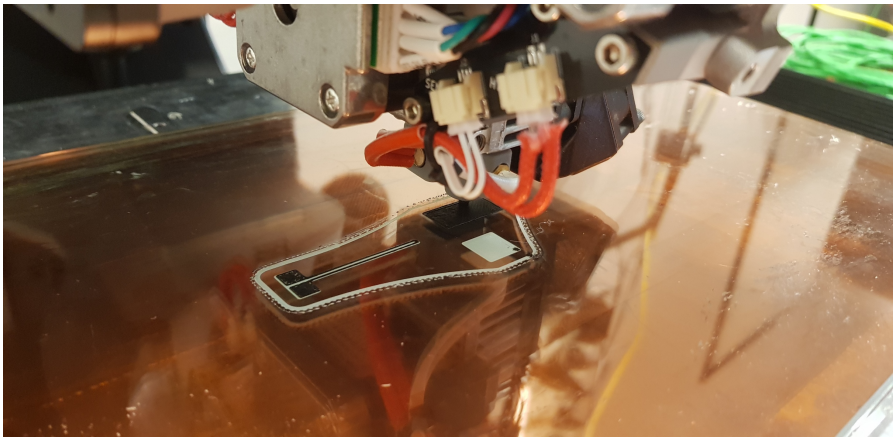

Figure 4.2: The 3D-printer, during the process of printing a sensor

Even with the discussed optimized settings, a part of the sensors had a short circuit, requiring multiple attempts to correctly print all sensors. The final prints can be seen in figure 4.3.

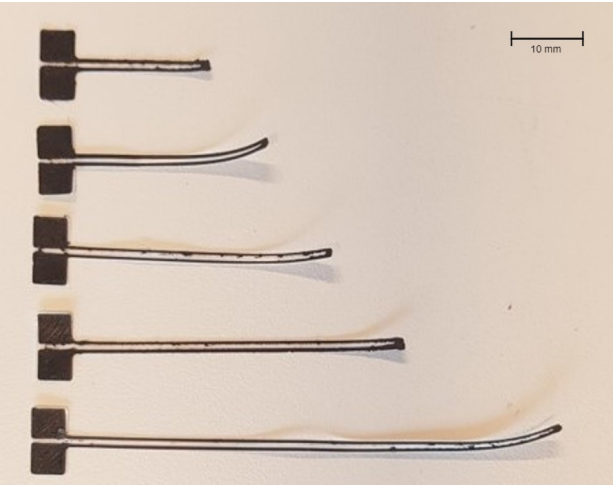

Figure 4.3: The final printed sensors

4.3 Post processing the prints

In the hours after the printing, the sensors showed the tendency to curl up. The start of this process can be seen in figure 4.3, which is taken just after printing. After a day, the sensor looked as in figure 4.4. The suspected cause for this, is difference in thermal expansion coefficients for the two materials.

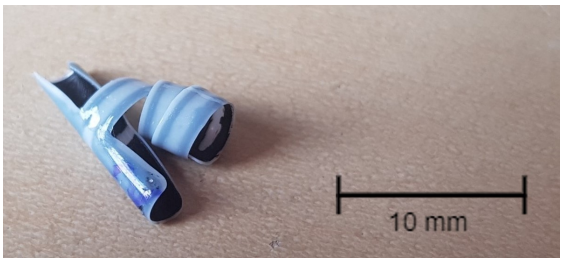

Figure 4.4: Curled sensor, $L = 30\,\text{mm}$

To prevent this from happening, the sensors were put in between two glass plates, immediately after the printing. This way, they could not curl up. After that, these glass plates with the sensors were put in an oven at 140 °C, for one hour. By increasing the temperature, the material softened and the accumulated internal stress was released. This can be seen as a way of annealing. After this process, the sensors showed no tendency to curl anymore. To make sure that they would stay straight, they are stored and transported in a stamp album.

Since it is not possible to directly solder wires to the sensor, wires are connected to the sensors by first soldering them to a piece of copper tape of the brand 3M [42]. This tape has a width of 6.35 mm and a thickness of 66 µm, which is then pasted to the contacts of the sensor. Conductive silver paint from Electrolube [43] is used to make sure the tape and sensor make good electrical contact. This way of connecting has earlier been used by Bernard Prakken in

his BSc assignment at RaM [44]. With the first batch of sensors fabricated, it was found out that this connection was not very reliable, so for the second batch, superglue is used to make the connection more enduring.

An example of a post processed sensor can be seen in figure 4.5. After the post processing was finished, the sensors have not been used for measurements in the first days, since they need this time to 'settle' and stabilize.

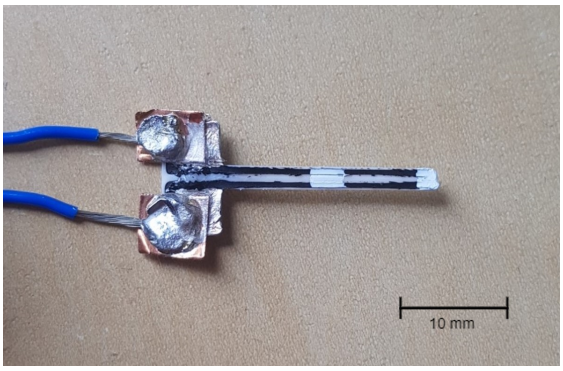

Figure 4.5: Post processed sensor, $L = 20\,\text{mm}$

4.4 Conclusion

In this chapter, the design is turned from a sketch in Solidworks into a printed and ready to use sensor. The printing process was an iterative process, during which the design had to be changed slightly. The optimal printing settings for these prints are discussed, as well as the post processing, necessary to prevent curling. Two batches of sensors are fabricated. The next chapter will elaborate on the measurements with these sensors.

5 Measurement methods

5.1 Introduction

This chapter is about the measurement set-up and methods that are used to do measurements with the fabricated sensors. First, the measurement set-up for the resistance measurement will be covered and subsequently the different kinds of wind tunnel measurements that are executed will be elaborated on.

5.2 Resistance measurement

An FRDM K64F micro-controller [45] is used to take measurements with the sensors. This is a 16-bit micro-controller with an Arduino-like pin layout. Code for this micro-controller is written in Mbed [46], a C++ platform, to read an analog input at a sampling frequency F_s of 4 kHz. This input is then converted with a built-in ADC converter and sent to the connected PC via serial communication. To measure the resistance of the sensor, generally a voltage divider is used, but a set of measurements is done with a Wheatstone bridge as well for comparison. The maximum voltage on an analog input is 3.3 V, which is thus the limiting factor for the measurements. On the micro-controller, only the voltages are measured. Matlab has been used to further analyse the data.

5.2.1 Voltage divider

A voltage divider is used for measuring the resistance, as can be seen in figure 5.1.

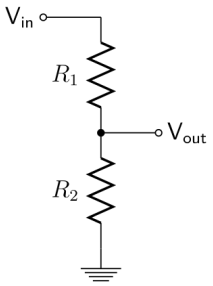

Figure 5.1: A voltage divider with two resistors [47]

Here R_1 is a known resistor and R_2 is the unknown resistor, in this case the strain gauge. V_{in} is a known input voltage and V_{out} is measured with the micro-controller. The relation between V_{in} and V_{out} is then described by the following equation, which is derived from Ohm's Law ($V = IR$):

$$V_{\text{out}} = \frac{R_2}{R_1 + R_2} V_{\text{in}} \tag{5.1}$$

This equation can be rewritten to find an expression for the unknown resistance R_2 as a function of the ratio between V_{out} and V_{in}:

$$R_2 = \frac{R_1 \frac{V_{out}}{V_{in}}}{1 - \frac{V_{out}}{V_{in}}} \tag{5.2}$$

All sensors in the first batch have a resistance in the order of magnitude 10^4 Ω, as can be seen in section 6.2. It was therefore decided to use a resistance of 10 kΩ for R_1. For the input voltage, the VCC of the Micro-controller is used, yielding a value of 3.3 V for V_{in}.

5.2.2 Wheatstone bridge

A Wheatstone bridge [48] is made as well to measure the resistance, in order to compare this to the voltage divider. A Wheatstone bridge in its essence is a combination of two voltage dividers, with 3 known and 1 unknown resistors. The difference of the output voltages of these voltage dividers is measured and used to compute the unknown resistor. A schematic overview of this can be seen in figure 5.2.

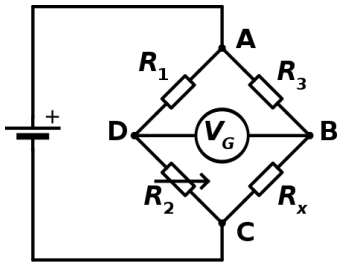

Figure 5.2: A Wheatstone bridge [48]

If all four resistors have the same resistance, $V_G = 0$ V. A change in one of the four resistances, in this case the strain gauge, will then have a relatively high effect on the change in V_G. For this setup, R_2 is the resistance of the strain gauge. R_1, R_3 and R_x are identical and as close to R_2 as possible. The ratio between V_{in} and V_G is then described by the following equation [48]:

$$V_G = \left(\frac{R_2}{R_1 + R_2} - \frac{R_x}{R_x + R_3} \right) V_{in} \tag{5.3}$$

This can be rewritten to calculate R_2 as a function of the ratio $\frac{V_G}{V_{in}}$:

$$R_2 = \frac{R_1 \left(\frac{V_G}{V_{in}} + \frac{R_x}{R_3 + R_x} \right)}{1 - \frac{V_G}{V_{in}} - \frac{R_x}{R_3 + R_x}} = \frac{R_1 \left(\frac{V_G}{V_{in}} + \frac{1}{2} \right)}{\frac{1}{2} - \frac{V_G}{V_{in}}} \tag{5.4}$$

The advantage of the Wheatstone bridge with respect to the voltage divider, is that the neutral value of V_G is around zero for the Wheatstone bridge. Thus, only the change in voltage is measured, which gives a much larger range to measure in, because then only the voltage difference is limited by the maximum input voltage of the micro-controller, not the voltages on points D and B themselves. With the voltage divider, the measured voltage is around half

the input voltage in neutral state if $R_1 = R_2$, which reduces the measuring range.

However, it is not possible to measure a voltage difference on the micro-controller. Thus, both V_D and V_B had to be measured with respect to the ground. Now these two values are limited by the maximum voltage of the micro-controller, giving a similar range as the voltage divider.

The Wheatstone bridge has eventually only be used to do measurements with the 20 mm long sensor from the second batch. This sensor was measured to have a resistance of 23.3 kΩ (see section 6.2). A resistor value of 22 kΩ is used for R_1, R_3 and R_x. Since all four resistor values are similar, the input voltage could be increased up to 6 V, without V_G getting higher than 3.3 V. This is done using an external voltage supply.

5.3 Wind tunnel

For the wind tunnel measurements, the University of Twente's educational wind tunnel [49] is used. This is a small-scale wind tunnel that can easily produce wind speeds of 16 $m s^{-1}$, which is the maximum flying speed of the Robird [2]. This wind tunnel can be controlled from a computer, on which the real-time flow data can be read, as well as the angle of attack. A schematic overview of the measurement set-up used for the wind tunnel tests can be seen in figure 5.3.

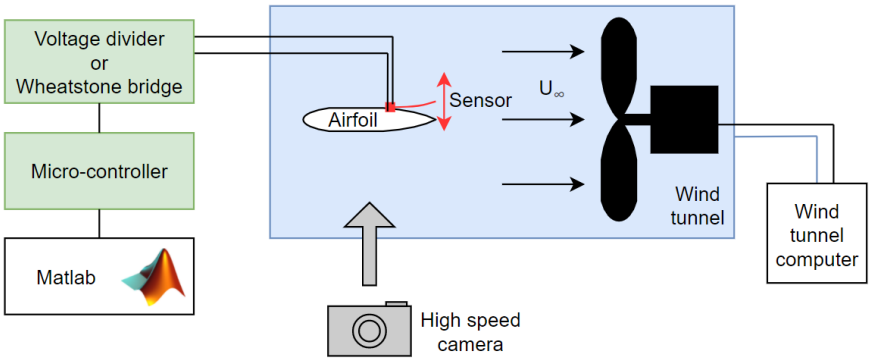

Figure 5.3: The measurement set-up for the wind tunnel tests.

The free stream velocity has an accuracy of 0.3 $m s^{-1}$ in both steady conditions as well as stall, so higher accuracy cannot be guaranteed. For the angle of attack, which had to be adjusted manually, the accuracy is about 0.1°.

Since the Robird's maximum flying speed is 16 $m s^{-1}$, it was chosen to take a free stream velocity of 10 $m s^{-1}$ for the measurements. In reality, the Robird will not fly constantly at its maximum speed, so this is considered to be a representative wind speed for the real situation.

5.4 High speed video analysis

To verify the mechanical behaviour of the sensor, a Casio EX-F1 high speed camera [50] is used. This camera is able to take videos at 300 fps, a frequency high enough to record the fluctuations in the sensor. These videos are then be analyzed in Kinovea [51], an open-source video player that offers a set of tools to analyse videos. This is used to gather knowledge about the mechanical behaviour of the sensors. Using the high-speed camera, videos are made of the different sensors in flapping state, which then are analysed in Kinovea. To improve the contrast with the dark background, white dots were put on the sensors. Specifically these dots are tracked.

5.5 Measurement types

A few different types of measurements are done in the wind tunnel. The sensor was put as far as possible to the trailing edge, but in such a way that it was still totally on top of the airfoil, as can be seen in figure 5.4. A piece of tape is used to keep the sensor in its place. All the measurements discussed in this section have a duration of 5 s, which is long enough for the sensor to show its fluctuating behaviour, but short enough to not give a very large amount of data at $F_s = 4\,\text{kHz}$.

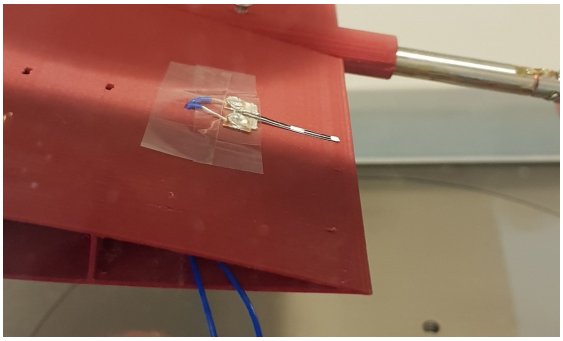

Figure 5.4: A sensor put on the back of the airfoil

5.5.1 Influence of angle of attack

The first set of measurements is done, in which the AOA is varied, such that both the aeroelastic and electrical behaviour of the sensor can be analysed at both laminar flow and stall. This way, it can be seen if there is a clear distinction between those two states, or that there might be a transition. These measurements are done for a constant free stream velocity of $10\,\text{m}\,\text{s}^{-1}$. During these measurements, the aeroeleastic behaviour of the sensors is determined based on visual effects, as well as a few reference high-speed videos are taken.

5.5.2 Influence of free stream velocity

Another set of measurements is done, where the AOA is kept constant, but now the flow velocity is changed in a range from 0 - $16\,\text{m}\,\text{s}^{-1}$, i.e. in the range of flying velocities that the

Robird has. This is done to see if the velocity has an effect on the behaviour of the tuft. These measurements are done for $\alpha = 10°$ (no stall) and $\alpha = 16°$ (stall).

5.5.3 Tribo-electric effect

A third measurement has been done to investigate the tribo-electric effect. This effect implies that two materials, when brought into contact with each other and then separated, get an electrical charge [52], which would disturb the resistance measurements. This could possibly occur when the sensor is in contact with the airfoil. To test this hypothesis, a measurement is executed with the 50 mm sensor of the second batch. The sensor was stuck on the trailing edge of the airfoil, in such a way that only the contacts are on the airfoil and the sensor itself trailing behind it. This measurement is done at $\alpha = 7.5°$ and $\alpha = 16°$. A free stream velocity of $10\,\mathrm{m\,s^{-1}}$ is used for this measurement.

5.5.4 Additional tests

Lastly, additional tests are done outside the wind tunnel. Here, the sensor was taped to the edge of a table, such that it hung vertically. For this, the sensor with the length of 20 mm is used, as this was expected to give the highest resistance change as function of bending angle, as elaborated on in section 3.6.2. Four cases are analysed: 1) no movement in the sensor at all, 2) an initial force applied, after which the sensor was left vibrating in its resonance frequency, 3) an initial bending of about 90 degrees after which the sensor was slowly bent back and 4) wind blown against the sensor, which caused it to vibrate. To analyze if the voltage divider caused problems, these cases are as well analyzed with a Wheatstone bridge.

5.6 Data analysis

To get an overview of the results of the measurements, basic statistical parameters such as mean and standard deviation have a central role. Next to that, the data is analysed in the frequency domain, using the fast fourier transform (FFT) and the power spectral density (PSD). The energy of the signal is calculated as well, by taking the integral over the whole frequency spectrum. Since the resistance data has unit Ω, the unit of the FFT has unit Ω s. When integrating over frequency, the unit Ω s Hz is obtained, or simply Ω. The unit of the energy of the signal is thus Ω.

A few times a low-pass filter is applied to the signal to filter out the higher frequency noise. This is done using the inbuilt signal analyser in Matlab. For this, the passband frequency and the steepness are mentioned at the specific locations in chapter 6 were filtered data is shown. Here, the steepness s is a scalar between 0.5 and 1 such that the transition width W of the filter is calculated as [53]:

$$W = (1 - s)(f_{\text{Nyquist}} - f_{\text{passband}}) \tag{5.5}$$

Here, $f_{\text{Nyquist}} = \frac{F_s}{2}$.

5.7 Conclusion

Different parts of the measurement set-up are discussed in this chapter. Firstly, the concepts of the voltage divider and the Wheatstone bridge are explained. Next, the set-up of the wind tunnel and high speed camera are briefly mentioned. Lastly, the different types of data analysis that are applied are mentioned.

6 Results

6.1 Introduction

This chapter presents and analyses the data that is gathered from the measurements. First, the electrical and aeroelastical characterisation of the sensors will be shown. Then, the results of the video analysis will be shared. Next, the results of the different measurements tests will be shown and discussed.

6.2 Electrical characterisation

The fabricated and post processed sensors are characterised by measuring the resistance in the straight state with a Fluke 170 digital handheld multi-meter [54]. The results of this can be found in table 6.1. These resistances are determined at an accuracy of 0.1 kΩ, except for the 40 and 50 mm sensors in batch 2, which showed an inaccuracy of respectively 5 and 1 kΩ.

Length (mm)	20	30	40	50	75
Batch 1: Resistance (kΩ)	21.0	49.1	53.6	14.0	73.6
Batch 2: Resistance (kΩ)	23.3	33.5	130	137	108.0

Table 6.1: Resistance measured with multi-meter, for sensor with various lengths

In figure 6.1, these resistances are plotted. For reference, the resistance calculated according equation 3.3 is plotted as well, with ρ fitted to be 0.025 Ω m. It can be seen that the relation between length and resistance values is not as linear as theory describes. It has to be noted that the theoretical resistance is that of the strain gauge only. The resistance of the contacts is not included in the calculations in section 3.6.2.

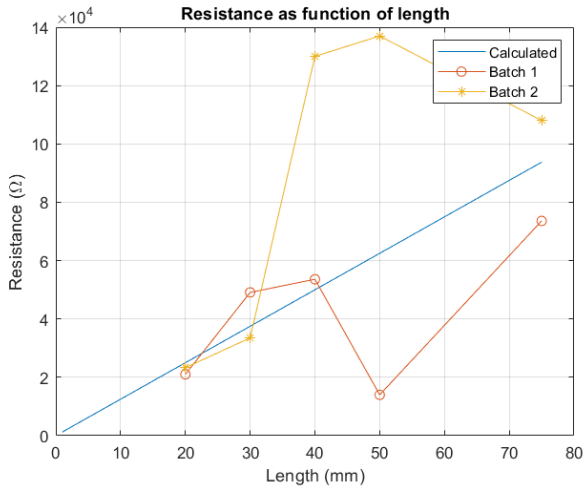

Figure 6.1: Resistance as function of length, calculated and measured

6.3 Aeroelastical characterisation

The length of the sensor has an effect on its aeroelastical behaviour, as the wind tunnel tests have shown. Four distinct states in which the sensor can be are identified. In the first state there is no movement at all. This is the case when there is no stall. When there is stall, other states are possible. In the second state the sensor behaves like a cantilever beam, which has a deflection in 1 dimension only: the vertical direction. In the third state unpredictable swishing occurs in which the sensor lashes out in all directions. This is usually followed by the fourth state, in which the flow reversal is strong enough to reverse the sensor. In the first set of measurements the aeroelastic behaviour of the sensors is determined visually. In table 6.2 an overview is given in which the response of the sensors to different angles of attack is shown for a free stream velocity of $10\,\mathrm{m\,s^{-1}}$. In figure B.1 in the appendix, for each state a snapshot from the video analysis is given.

The Cauchy numbers as calculated in section 3.6.3 are included in the table as well. It can be concluded that for $Ca \leq 10^3$ the beam assumption holds. For $10^3 < Ca < 10^4$ there is a transition where the tuft behaves like a beam until the forces in the fluid become too large and for $Ca > 10^4$ the tuft does no longer behave like a beam. This means that the fluid properties are dominating with respect to the elasticity of the solid.

Length (mm)	20	30	40	50	75
Cauchy number	424.35	1432.2	3394.8	6630.5	22378
No movement	$\alpha < 12.5$	$\alpha < 12$	$\alpha < 12$	$\alpha < 12$	$\alpha < 12$
1D flapping	$\alpha \geq 12.5$	$\alpha \geq 12$	$12 \leq \alpha < 13$	$\alpha = 12$	-
Swishing	-	-	$13 \leq \alpha < 14$	$12 < \alpha < 13$	$12 \leq \alpha < 13.5$
Reversed	-	-	$\alpha \geq 14$	$\alpha \geq 13$	$\alpha \geq 13.5$

Table 6.2: Aeroelastical behaviour of the sensors, $U_\infty = 10\,\mathrm{m\,s^{-1}}$

For $L = 50\,\mathrm{mm}$, there is a sudden transition at $\alpha = 12°$. To clarify this a video on this is accessible via the hyperlink given in section 6.4.

6.4 Video analysis

For verification of the measurements videos are made of different situations, which are accessible via the following hyperlink: https://bit.ly/3xMV3z2. A few screen shots from these videos are visible in appendix B.

A few of these videos are made with the high speed camera discussed in section 5.4. These videos are analyzed in more detail using Kinovea. As can be seen from table 6.2, the sensors with lengths of 20 and 30 mm show 1D-flapping only. These were the only sensors for which Kinovea was able to track the white dot on the tip since the swishing of the other sensors made tracking impossible. The results of this video analysis can be found in figure 6.2.

A base line was found in the displacement data, which has occurred because there was a drift present in Kinovea. Therefore, a high-pass filter is applied to the signal, with a passband frequency of 1.5 Hz and steepness of 0.75. Subsequently the PSD was estimated.

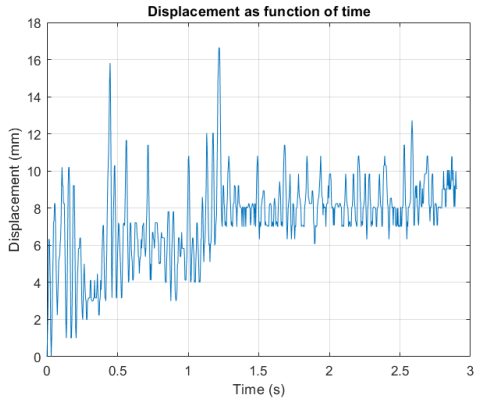

(a) Displacement, L = 20 mm

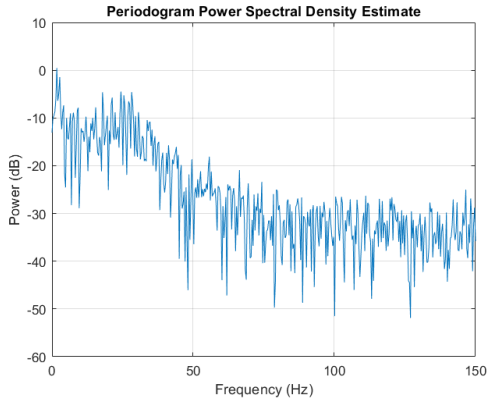

(b) PSD after applying high-pass filter, L = 20 mm

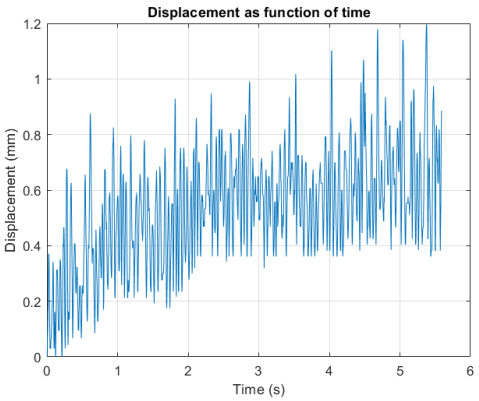

(c) Displacement, L = 30 mm

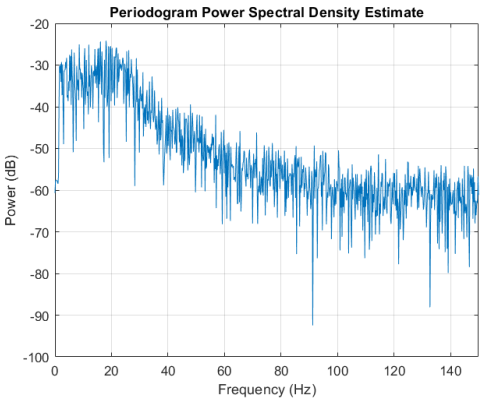

(d) PSD after applying high-pass filter, L = 30 mm

Figure 6.2: Displacement data and PSD estimate, for sensors with L = 20 mm and L = 30 mm. $U_\infty = 10\,\mathrm{m\,s^{-1}}, \alpha = 16°$

It can be seen that for both of the analyzed sensors, a broad peak appears in the frequency spectrum, at around 20 Hz, which in the videos can be seen to be the flapping frequency. Although it can not be determined accurately, for the other videos the flapping or swishing appears to be at approximately this same frequency. Since this frequency is constant for at least two but presumably all of the different lengths, it probably is not determined by the sensor characteristics, but rather by the properties of the aerodynamics or the interaction between airflow and solid.

There is another aspect that can be seen from some of the videos as well. When the sensor bent in the span-wise direction, e.g. when it was swishing around or in reversed state,

it never bent in the outward direction but always in the direction of the middle of the wing. This proves the existence of the 3-dimensional effects that were discussed in section 3.7.

6.5 Wind tunnel tests

6.5.1 Initial wind tunnel test

With the first batch of sensors, wind tunnel test as described in section 5.5.1 are executed to get an impression of the electrical behaviour. For this, the wind speed was set to $10\,\mathrm{m\,s^{-1}}$ and measurements were done for angles of attack in a range from 10° to 14°.

The sensors turned out to be faulty, as a result of which the ratio $\frac{V_{out}}{V_{in}}$ reached 1 sometimes. This means that the resistance of the tuft is infinite, as can be calculated with equation 5.2. This is of course not the case in reality, so the only logical explanation is that the contacts of the sensors were not enduring enough. For the sensors with lengths of 20, 40 and 50 mm, this could be fixed at site and the measurements were redone. However, for the 75 mm, $\frac{V_{out}}{V_{in}}$ still reached 1 occasionally. Therefore, it was not possible to calculate the resistance, as a result of which only the ratio $\frac{V_{out}}{V_{in}}$ is analysed here. The average values, standard deviations and energies of these signals are plotted in figure C.1 in appendix C. For the sensor of 30 mm, this was slightly folded during transportation and therefore no measurement could be done with it.

Due to the fact the quality of this first batch of sensors cannot be guaranteed, no conclusions are based on these data.

6.5.2 Influence of angle of attack

The measurements as discussed in section 5.5.1 are executed with the second batch of sensors. For every sensor a reference measurement is done, where the sensor was in the same conditions as during the tests, with the only difference that the wind tunnel was not turned on, to investigate the effect of the wind on the measurements. These reference data can be found in table 6.3. For comparison, the determined resistances from the multi-meter measurement (see section 6.2) are shown as well.

Length (mm)	20	30	40	50	75
Multi-meter resistance (kΩ)	23.3	33.5	130	137	108.0
Average resistance (kΩ)	29.69	35.49	120.6	178.8	126.8
Standard deviation (kΩ)	0.38	0.74	4.5	8.8	5.7
Energy (kΩ)	76.71	126.7	649.8	1264	823.1

Table 6.3: Reference data for all five sensors, $U_\infty = 0\,\mathrm{m\,s^{-1}}$

For the sensor with a length of 50 mm, a part of the resistance data is plotted as a function of time, for $\alpha = 10°$ and $\alpha = 16°$. This can be seen in figure 6.3. A low-pass filter with a passband frequency of 100 Hz and a steepness of 0.85 is applied to the signal. In figure 6.4 a part of the filtered signal can be seen.

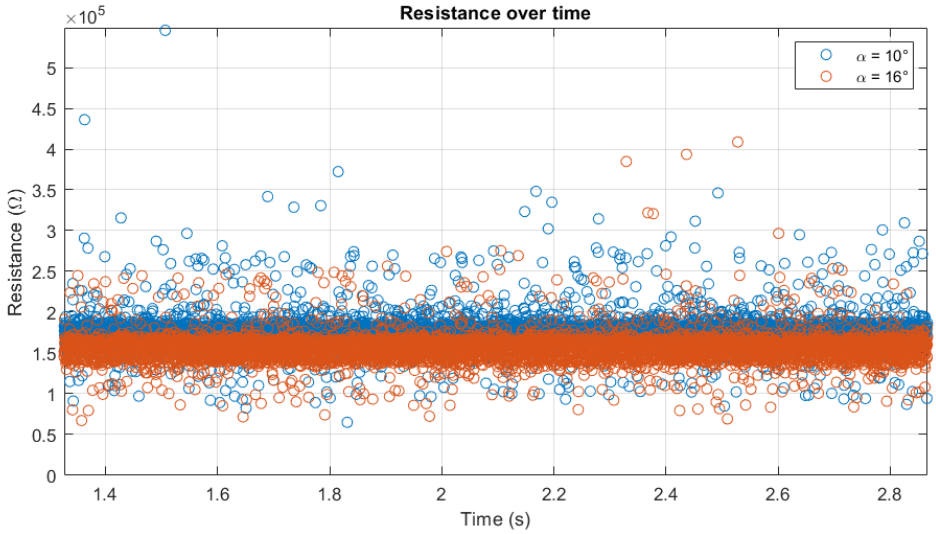

Figure 6.3: Resistance over time for L = 50 mm, measured for $\alpha = 10°$ and $\alpha = 16°$

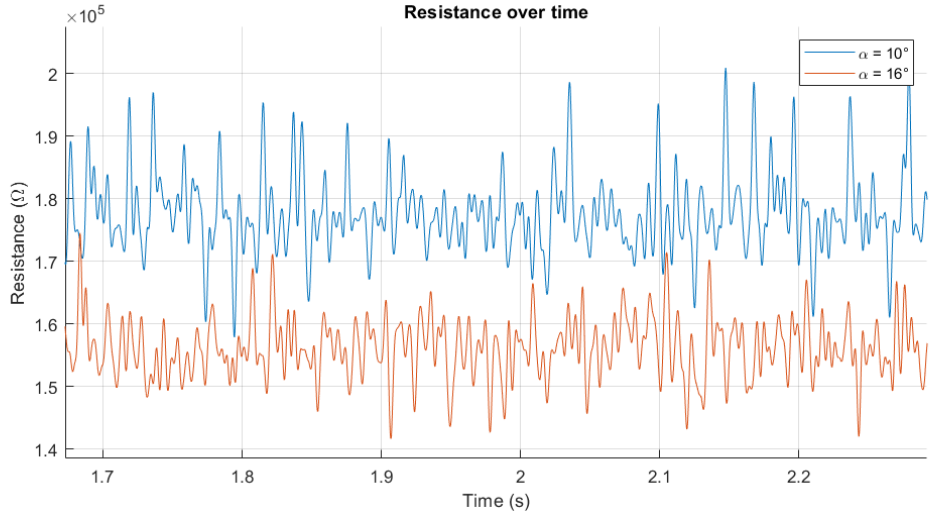

Figure 6.4: Resistance over time for L = 50 mm after applying a low-pass filter, measured for $\alpha = 10°$ and $\alpha = 16°$

It can be clearly seen that there are no low-frequency fluctuations in the data for $\alpha = 16°$, whereas that would be expected due to the flapping behaviour of the sensor. The other sensors show similar results: the signal is rather constant with a lot of noise. No differences are identified between laminar flow and stall, except for a change in average resistance. For the other sensors, low-pass filtering is applied as well, but with the same result as for the 50 mm sensor.

Since the goal of this project is to measure qualitatively only, and it gives a better overview, the data gathered from the measurements are plotted relative to the reference data from table 6.3. This can be seen in figure 6.5.

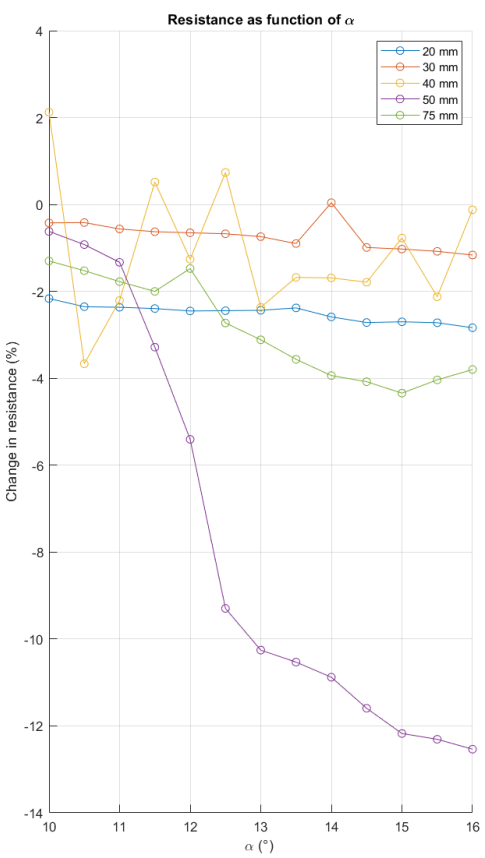

(a) Relative resistance

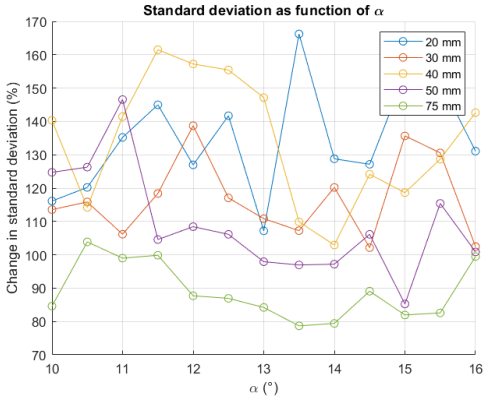

(b) Relative standard deviation

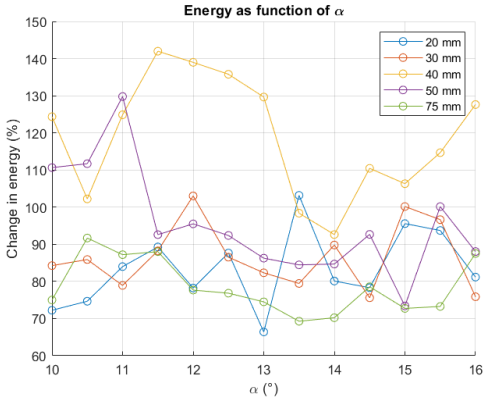

(c) Relative energy

Figure 6.5: Resistance, standard deviation and energy of the five sensors, plotted with relative to the reference values, for $U_\infty = 10\,\mathrm{m\,s^{-1}}$

Looking at the average resistance of the sensors, it can be seen that this is generally a few percent lower than when the wind tunnel is turned off, but this is not a large difference. What can be seen, is that all sensors but the one of 40 mm show a decrease in resistance when stall occurs, due to the bending of the sensor. Especially for the longer ones, 50 and 75 mm, it can clearly be seen that there is a turning point at $\alpha = 12°$. Compared to table 6.2, these are the sensors that show (almost) only swishing behaviour. This thus decreases the average resistance more than the 1D-flapping only.

The standard deviation and the energy of signal can be seen to increase by 70 to even 160 %, just by turning the wind tunnel on. No visual changes were noticeable: as long as there was no stall, the sensors were nicely adjacent to the airfoil. However, apparently, the wind did induce a large amount of noise in the signal. Since no fluctuations are visible in the resistance data for any length and AOA, the increased standard deviation has to be due to noise only.

From these data, no clear differences can be found between the situation for $\alpha < 12°$ (no stall) and $\alpha \geq 12°$ (stall). This is in contradiction with what was concluded in section 6.5.1. It was expected that the flapping of the tuft would induce larger changes in resistance, and that the flapping frequency would be visible when the frequency spectrum of the signal would be plotted by estimating the power spectral density. However, that was not the case either, the frequency spectrum only showed a lot of noise over the whole spectrum, as can be seen for the sensor with length 50 mm in figure 6.6. Here, no difference between stall and no stall is identified either.

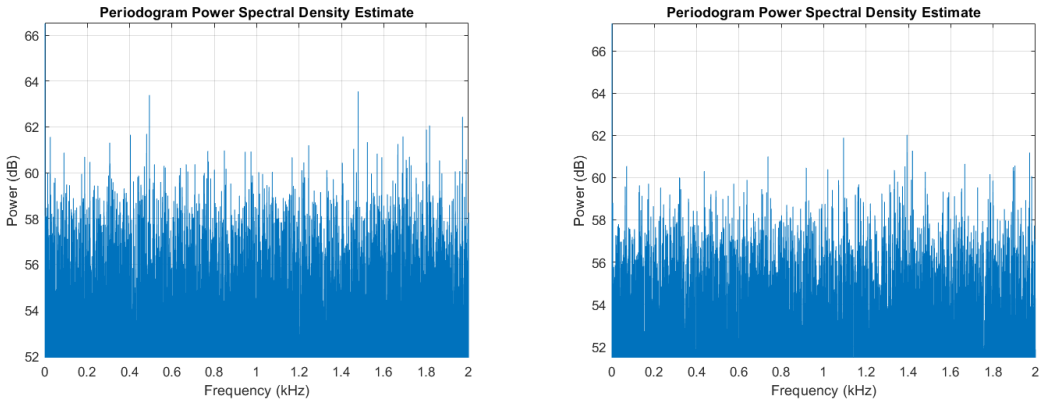

(a) PSD estimate ($\alpha = 10°$)

(b) PSD estimate ($\alpha = 16°$)

Figure 6.6: PSD estimate for $L = 50$ mm, measured for $\alpha = 10°$ and $\alpha = 16°$.

It has to be concluded from this, that there is no clear difference in standard deviation between stall and no stall. The different states from table 6.2 cannot be identified in the resistance data. More measurements are executed to find an explanation for this unexpected behaviour, which are shown in the next sections. However, in general the average resistance is shown to drop by a few percent, specifically for the larger sensors, when stall occurs.

6.5.3 Influence of free stream velocity

With the sensor with length 50 mm, a separate measurement is done to investigate the effect of the free stream velocity, as described in section 5.5.2. This is measured at $\alpha = 10°$ (no stall) and $\alpha = 16°$ (stall). Via the hyperlink given in section 6.4, a few high speed videos can be found on the behaviour at stall, for different lengths. However, it was not possible to analyse these in Kinovea, so no conclusions are based on them. The average resistance and standard

deviation can be found in figure 6.7.

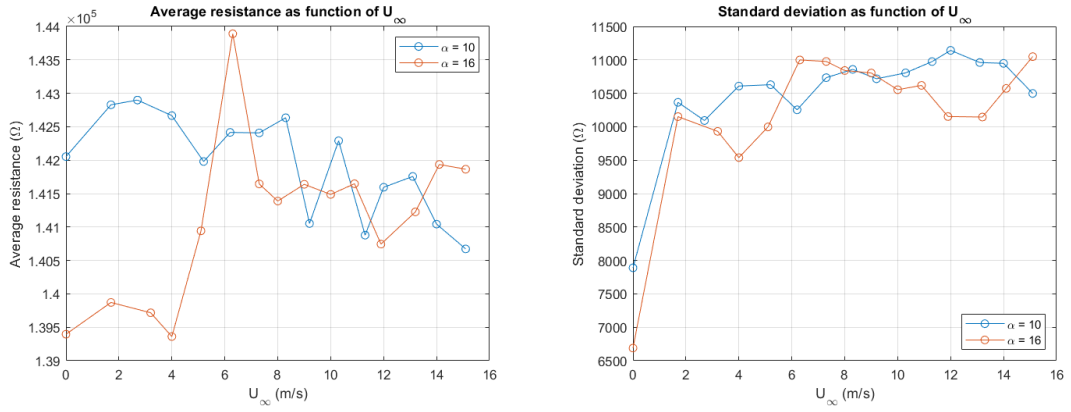

(a) Average resistance

(b) Standard deviation

Figure 6.7: Average value and standard deviation of the resistance, as function of the free stream velocity, measured for $\alpha = 10°$ and $\alpha = 16°$

A few things can be concluded from these results. First, it can be seen that the standard deviation is significantly lower when there is no flow ($U_\infty = 0\,\mathrm{m\,s^{-1}}$). This is in agreement with earlier tests and indicates that the flow itself has a large influence on the amount of noise in the signal, no matter if there is stall or not. When there is a flow, the standard deviation is generally about 1.5 times larger, it does increase a bit with increasing flow velocity. There is no significant difference between stall and no stall.

In figure C.1a, the average resistance can be seen to be lower at stall than at normal flow, for wind speeds up to $5\,\mathrm{m\,s^{-1}}$, for which an explanation has not yet been found. At larger speeds, the average resistance does not change much, although a small decline with increasing U_∞ can be identified. At $U_\infty = 10\,\mathrm{m\,s^{-1}}$, the average resistance at stall is lower than when there is no stall, which is in agreement with the results from section 6.5.2. However, this could be very well a coincidence.

6.5.4 Tribo-electric effect

A possible explanation for the high noise in the signals measured in the wind tunnel could be the tribo-electric effect. For both a situation without stall ($\alpha = 7.5°$) and a situation with stall ($\alpha = 16°$) a measurement is taken with the sensor with length = 50 mm, as described in section 5.5.3, of which the results can be seen in table 6.4. Of both situations, a video is made for reference, which is accessible via the link given in section 6.4. A part of the resistance data as function of time can be seen in figure 6.8.

In figure 6.9, the power spectral density estimate for both cases can be seen. These look quite similar, there are no frequencies that appear to have a peak at only one of the two.

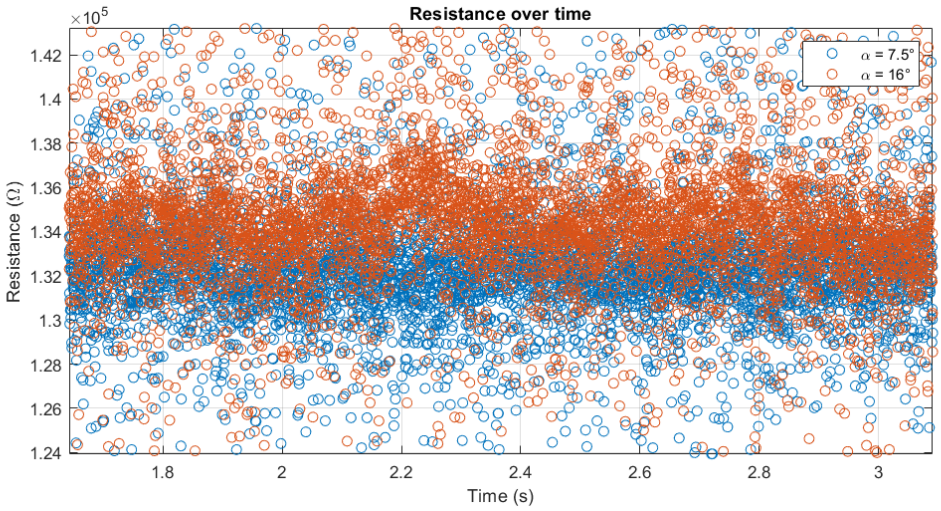

Figure 6.8: Resistance as function of time for a sensor with L = 50 mm at the trailing edge, for $\alpha = 7.5°$ and $\alpha = 16°$

	$\bar{R}$ (kΩ)	σ (kΩ)	E (kΩ)
No stall: ($\alpha = 7.5°$)	132.7	6.3	919.4
Stall: ($\alpha = 16°$)	135.1	7.0	1010.1

Table 6.4: Average resistance ($\bar{R}$), standard deviation (σ) and energy (E) of a sensor on the trailing edge of a wing. $L = 50\,\text{mm}$, $U_\infty = 10\,\text{m}\,\text{s}^{-1}$

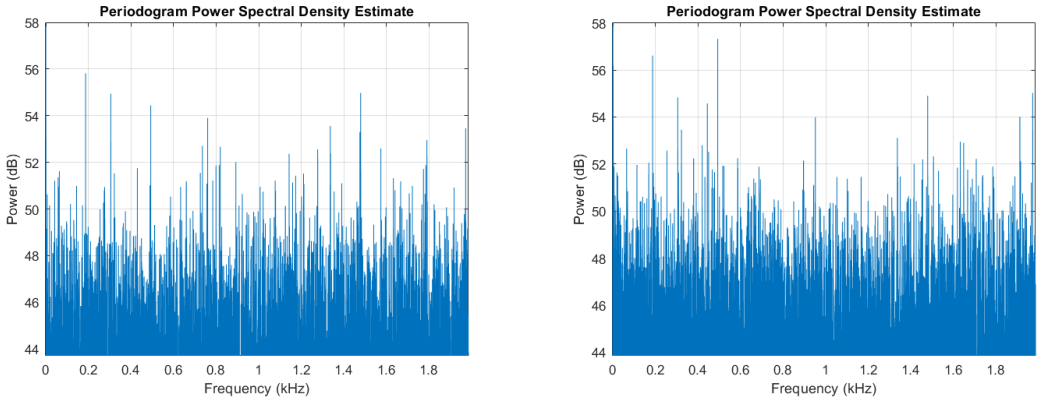

(a) Power spectral density estimate - no stall

(b) Power spectral density estimate - stall

Figure 6.9: Power spectral density estimate for a sensor on the trailing edge of a wing

Due to the fact that the sensor is now in the wake of the airfoil, the sensor is now in flapping state as well when no stall is occurring. Despite that, the standard deviation at stall is still 10 % higher than without stall. In both cases the standard deviation is about 6 kΩ, which

is actually lower than the standard deviation measured for $U_\infty = 0\,\mathrm{m\,s^{-1}}$ for this sensor, in section 6.5.3. Due to the fact that wind is present, as well as a lot of flapping, it would make sense that a higher standard deviation would be found.

Despite the lower standard deviations, the fluctuating behaviour is not visible in the resistance data here either, as can be seen from figure 6.8. Although no further research is done towards this specific topic, it is therefore concluded that the tribo-electric effect cannot be confirmed or ruled out based on these measurements and would definitely be worth looking into in more detail.

6.6 Additional tests

The wind tunnel tests did not show the expected result. There was not a clear, indisputable difference in resistance data between stall and laminar flow. To gain more information on why this is the case, a few more tests are done, outside the wind tunnel, as described in section 5.5.4. The results of these tests can be seen in figure 6.10. The average resistance, standard deviation and energy can be found in table 6.5.

	Wheatstone bridge			Voltage divider		
	$\bar{R}$ (kΩ)	σ (kΩ)	E (kΩ)	$\bar{R}$ (kΩ)	σ (kΩ)	E (kΩ)
No movement	23.82	0.078	55.90	23.66	0.065	54.46
Initial force	24.01	0.097	57.88	23.73	0.109	56.83
Initial displacement	24.23	0.131	60.59	23.89	0.102	57.54
Blowing	24.03	0.107	57.22	23.91	0.126	57.11

Table 6.5: Average resistance ($\bar{R}$), standard deviation (σ) and energy (E) of a free hanging sensor outside the wind tunnel, in four different cases, measured with a voltage divider and a Wheatstone bridge

It can be seen that the resistance, measured with the voltage divider, is about 200 Ω lower than when it is measured with the Wheatstone bridge. This is constant throughout the four cases and therefore not a problem, as the analysis is only qualitative. No further differences are seen between the voltage divider and the Wheatstone bridge, as a result of which it can be concluded that, compared to the Wheatstone bridge, the voltage divider does not have an influence on the accuracy of the signal, apart from the slightly increased resolution due to the fact that a higher input voltage is used, as discussed in section 5.2.2. However, if it would have been possible to measure the voltage difference in the Wheatstone bridge directly, it might have been more accurate, as discussed in section 5.2.

Looking at the fist case (figure 6.10a), it can be seen that the average resistance is similar to the reference value displayed in table 6.3. However, it can be seen that in that case, the standard deviation was 380 Ω, whereas here it is 78 Ω for the Wheatstone bridge and only 65 Ω for the voltage divider. What is more, this is the case in all four situations: the highest standard deviation is 131 Ω, almost three times lower than the reference value from the wind tunnel tests, which were taken at $U_\infty = 0\,\mathrm{m\,s^{-1}}$.

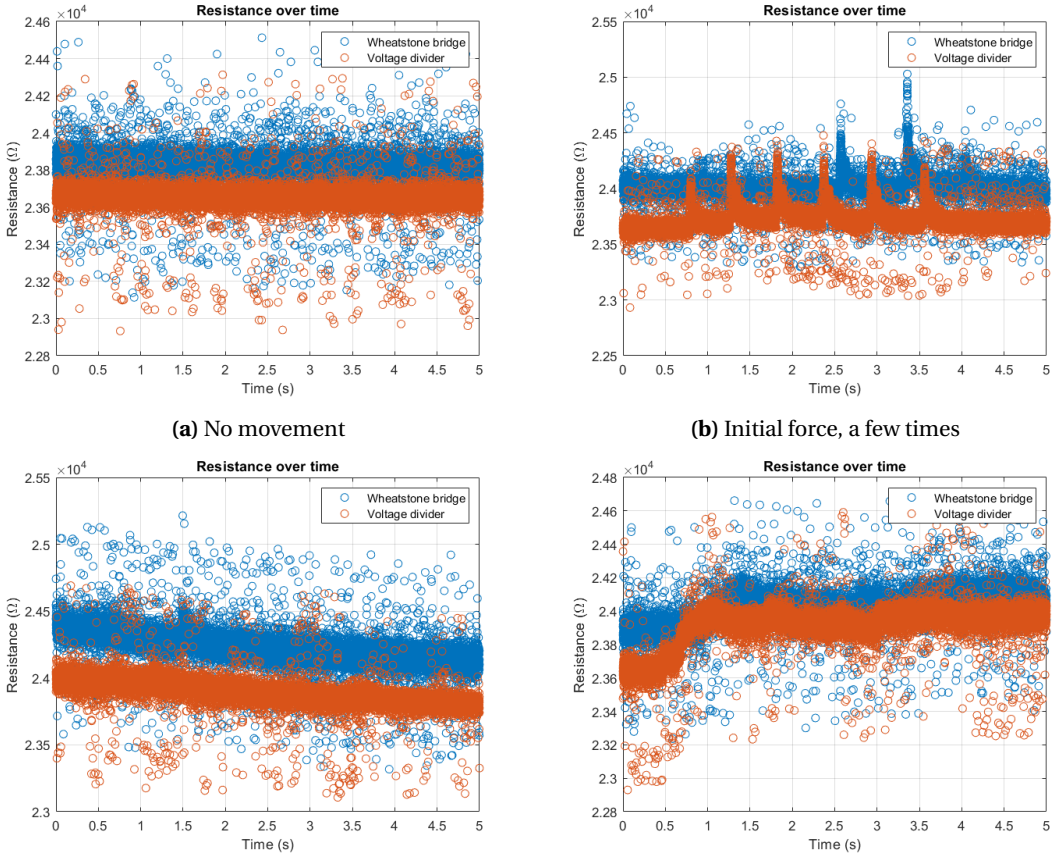

(a) No movement

(b) Initial force, a few times

(c) Initial displacement, slowly bent back

(d) Blowing

Figure 6.10: Resistance data in different circumstances, measured with both a voltage divider and a Wheatstone bridge

The second case shows quite clear results. In figure 6.10b, it can clearly be seen from the peaks when the force was applied. In figure 6.11a, a more detailed figure can be found of a part where clearly the fluctuations of the sensor can be seen. This fluctuations are found to happen at around 20 Hz, which is the same frequency found from the video analysis in section 6.4. Although it does not correspond with the eigenfrequency as shown in table 3.2, this is at least remarkable. It could be either be a coincidence, or an indication that the calculated eigenfrequencies are not correct, possibly due to the assumptions that were taken.

In the third case, figure 6.10c, clearly a decrease in resistance over time can be seen, due to the fact that the sensor was slowly bent back to its neutral state.

The fourth case is the one resembling the wind tunnel test the most, as here a little wind was blown against the sensor, to make it fluctuate. In figure 6.10d, it can clearly be seen that this blowing started after 0.5 s and continued to the end of the measurement. This can be

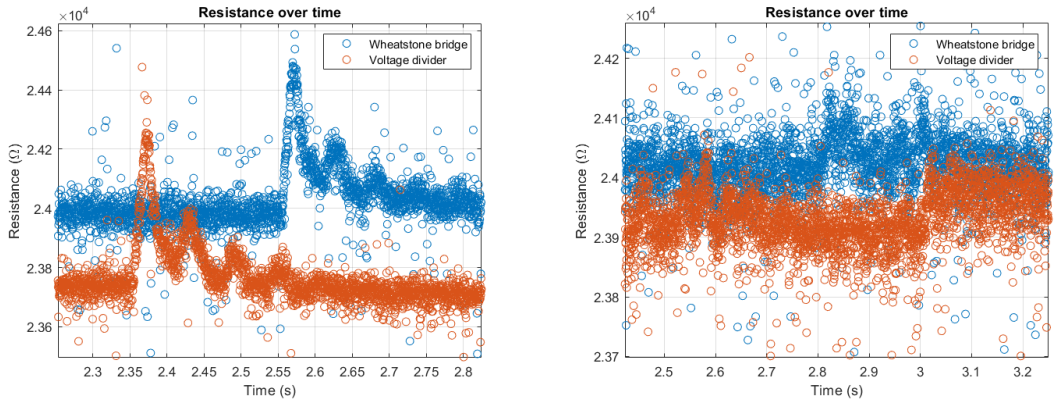

(a) Zoom of figure 6.10b

(b) Zoom of figure 6.10d

Figure 6.11: Detailed zoom of figures 6.10b and 6.10d

seen by an increase in resistance. However, the fluctuations that took place, made the sensor lash out to both sides of the neutral state, which would require the resistance to go alternating above and below the neutral value, at the frequency of the fluctuation. However, only an increase in resistance can be seen, which indicates a different response to compression and elongation. In figure 6.11b, a zoom on a part of the signal can be seen. From that, it can be seen that a little bit of fluctuation takes indeed place, but this is mostly drowned out by the noise of the signal. However, this noise is not larger than when no wind was blown. In the PSD, which can be seen in figure 6.12 many frequencies can be identified, but there is not a single flapping frequency that is clearly visible.

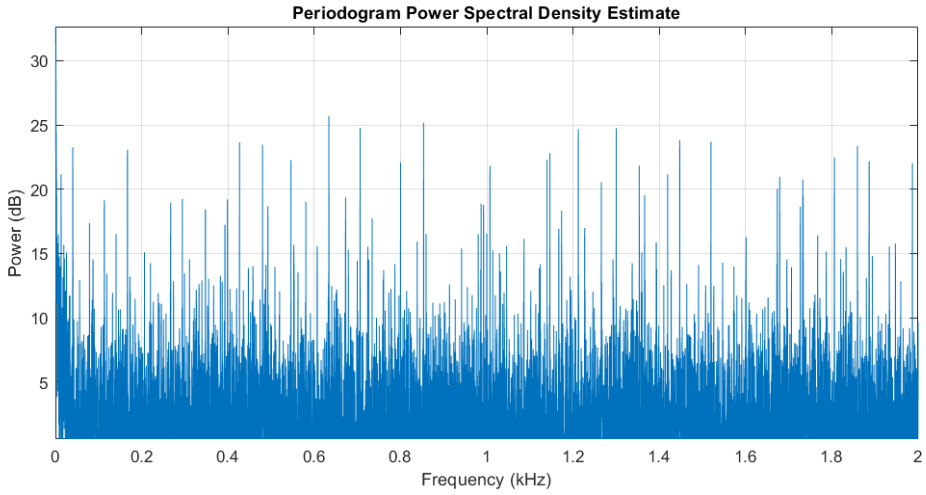

Figure 6.12: PSD estimate of the signal from figure 6.10d

When comparing figures 6.10b and 6.10d, it can be concluded that fluctuations due to wind are way less visible in the signal than fluctuations due to an initial force, although the stan-

dard deviation is comparable. This therefore has to be due to unknown properties of the wind. Since the standard deviation of the signals in the wind tunnel measurements were over 6 times larger, this proves that there was simply too much noise to distinguish the fluctuations clearly, even after filtering.

6.7 Conclusion

This chapter has described the results of the different measurements. First, the sensors are characterised electrically, by determining the resistances, and then aeroelastically, by investigating the different types of behaviour shown for different AOAs. It was found that the sensors of 20 and 30 mm behave like a beam, but the slenderness of the longer sensors eventually causes different behaviour, when the AOA is too large. Next, the results of the video analysis have been discussed, showing that the fluctuations occurred at a frequency spectrum around 15 - 25 Hz.

The different wind tunnel tests are elaborated on, which did not show a clear distinction between stall and no stall. Although there was generally a decrease in average resistance at stall, the fluctuating behaviour that was seen from the videos was not visible in the resistance data, due to the fact that the signal-to-noise ratio was too low. Changing the free stream velocity did not improve the visibility of the fluctuations. The tribo-electric effect is shown to be possibly a part of the problem. In the last section, more tests are done outside the wind tunnel. These showed that the fluctuations due to wind are less visible than the one due to an initial force. On top of that, it is shown that the standard deviation of the signals measured in the wind tunnel is around 6 times higher. In the next chapter, these effects will be discussed in more detail.

7 Discussion and recommendations

7.1 Introduction

In this chapter, the different parts of the project that are treated in this report, will be discussed. Where it turns out that some things could have been done better or different, recommendations for further research are given. The discussion is divided into four topics: the fabrication process, the measurement set-up, the aeroelastical working and the electrical working.

7.2 Fabrication

7.2.1 General fabrication process

The fabrication of the sensors was a iterative project. In the end, working sensors without short circuits were printed. However, still some sensors showed short circuits, as a result of which new ones had to be printed. To prevent this, the sensor could be made a bit wider, so that there is more distance between the two 'legs' of the sensor. This has the downside that it will increase the bending stiffness of the tuft. Another option would be to further analyze different printer settings in order to improve the accuracy of the printing.

Recommendation: refine the design or the printer settings to avoid short circuit.

7.2.2 Durability of contacts

As discussed before, the contacts of the sensors were not durable enough at first. This has been resolved with superglue, but this might still be a part of the cause of the noise in the signal. It should be investigated if the quality of the contacts can be increased.

Recommendation: investigate if it is possible to increase the quality of the contacts of the sensor

7.3 Measurement set-up

7.3.1 Resistance measurement

During this project, a voltage divider has been the major way to measure the resistance. As discussed, a Wheatstone bridge was built as well, to see if that made a difference. However, due to the limitations of the micro-controller, the voltage difference in the Wheatstone bridge could not be measured directly. The micro-controller was only able to measure voltages with respect to the ground, as a result of which two voltages had to be measured, of which the difference was the required voltage to calculate the resistance of the strain gauge. The micro-controller could only measure voltages up to 3.3 V, this meant that neither of the two voltages could get higher than this value. If the voltage difference could be measured directly, then only the difference would be limited by this 3.3 V. This allows to use higher voltages, with higher accuracy as a consequence. For further research, it is definitely worth looking into a

way to accomplish this.

Recommendation: look into possibilities to combine the micro-controller with a way to measure the voltage difference directly. An option would be to use a different kind of micro-controller or a shield, which is able to measure voltage differences

7.4 Aeroelastical working

7.4.1 Video-tracking

With the current sensors and the used software it was not possible to video-track the sensors when these showed swishing behaviour, as a result of which only the shortest two sensors could be properly analysed. However, if it would be possible to analyse the other sensors as well, more information could be gained on the mechanical behaviour of the sensors and the frequency of flapping. So, although it is a good tool to have used, it has not been exploited to its full potential.

Recommendation: investigate possibilities for video-analysis for the sensors that show swishing and reversion behaviour, for example by using a camera with a higher resolution or better software, or by making the end of the tuft thicker, such that it is better visible for the camera.

7.4.2 Stiffness

When designing the sensor, it was not certain if a sensor of these dimensions would show flapping behaviour, as it was not known how strong the forces at stall would be and if the stiffness of the tuft would be small enough. It can be concluded that this was definitely the case: not only do the sensors flap, they also show swishing and reversion. These effects are unpredictable, but show that the stiffness is small enough and could be increased if necessary, certainly for the longer sensors, without making the sensor too stiff. This could be useful as well, in order to make the longer sensors behave as cantilever beams and show 1D-flapping as well.

Recommendation: it is not necessary to improve the sensor on this field, but if it would be required to increase the sensor in size, it would be not a problem.

7.4.3 Effect of length

To investigate the effect of the length on the sensor, sensors with lengths of 20, 30, 40, 50 and 75 mm are designed. This has turned out to be useful, since the different lengths induce different behaviour, both mechanically as well as electrically. On the mechanical level, the shorter sensors, with lower Cauchy number, behave like a cantilever beam, whereas the longer ones show swishing and reversion. This swishing makes the movement unpredictable and not easy to video-track, but reduces the resistance by a greater amount, and is therefore better measurable. Due to time restrictions, not all measurements are executed with all different lengths. This is specifically the case for the additional tests outside the wind tunnel that are executed, and the test that has been done to look into the tribo-electric effect.

Executing these tests with different lengths would certainly be useful, since the sensors show different behaviour.

Recommendation: execute the measurements with sensors of all lengths.

7.5 Electrical working

7.5.1 Characterisation

As is seen in section 6.2, the relation between the length and the resistance is not as linear as calculated in section 3.6.2. This is most likely due to the fact that the strain gauge has such a small cross-section. Due to the fact that the thickness is only 0.1 mm, little inaccuracies in the printing have large consequences for the resistance value, and the accuracy of this. It is worth investigating if adding one or more layers on top of the current strain gauge, improves this.

With the current way of measuring it is not possible to know the resistance of the tuft and the contacts specifically. To investigate if the contacts have a large influence on the resistance, a four-point resistance measurement can be investigated.

Recommendation: it is recommended to make the cross-section of the strain gauge larger, specifically by adding one or more layers on top of this. It is also advised to investigate the resistance of the contacts of the sensors, by doing a four-point resistance measurement

7.5.2 Measurement results

The measurements show mixed results. On the one hand, there is a decrease in average resistance, as a result of the bending of the sensor. However, the fluctuations of the sensor in the wind tunnel cannot be seen in the resistance data, not even after applying a low-pass filter, but they can be seen when the measurements are taken outside the wind tunnel with manually applied initial forces or displacements. When blowing wind against it outside the wind tunnel, the fluctuation is again hardly visible. On top of that, the standard deviation in the signal with the wind tunnel turned on, is two times higher than when it is not turned on, which is again three times larger then when the sensor is not in the wind tunnel at all. Summarized in short: the fluctuations are visible in both the time and frequency domain, as long as there is no wind present. This gives the strong impression that the wind has properties that reduce the signal to noise ratio drastically.

On top of that, the tribo-electric effect could play a role, since it turned out that the standard deviation in the signal of the tuft on the trailing edge, was significantly lower than that of the same sensor on top of the wing, in the same conditions. However, the fluctuations of the sensor in those data were not visible either. It could be even the case that the tribo-electric effect is present because of the airflow as well, as it is possible to generate electricity from flutter-driven tribo-electrification [55,56]. The tribo-electric effect is thus worth looking into, and more measurements could be done with sensors on the trailing edge.

Recommendation: it is recommended to investigate ways to increase the signal to noise ratio of the signal, specifically in wind conditions. This could be done by enlarging the cross-sectional area, to have a more consistent signal, or by putting a strain gauge in the first part of the sensor only, instead of over the whole length of the sensor. Next, more research should be done into the tribo-electric effect.

7.6 Conclusion

On four main topics, the results are discussed and recommendations are given. The most important point of attention is the fact that the sensors showed to be capable of measuring deflections, but when wind is present the signal-to-noise ratio decreases drastically. Wind from the wind tunnel increases noise, whereas deflections due to blowing showed to be less visible than those to an initial force. Since the purpose of the sensor is to measure wind properties, this is a very important problem to solve.

8 Conclusion

This report has described the process of designing, fabricating and testing of a sensor to measure stall in a qualitative way. First, a theoretical framework is established, in which both static and dynamic aerodynamics are covered, as well as the fluid-solid interaction. With this knowledge, a tuft-like sensor with a piezoresistive strain gauge is designed. Lengths of 20, 30, 40, 50 and 75 mm are used, to investigate the effect of the length on the behaviour of the sensor. The Cauchy number is determined as an important measure for the fluid-solid interaction based on the slenderness ratio of the sensor. The resistance changes and eigen-frequencies are determined as a function of the length as well.

These sensors are 3D-printed using FDM and post processed in order to use them. A combination of a micro-controller and either a voltage divider or Wheatstone bridge is used to measure the resistance. Different tests are executed, both outside and inside the wind tunnel. In the latter case, the sensors have been placed on a customized NACA 0012 airfoil. The resistance is measured and videos are taken for reference. The short sensors behave like a cantilever beam, whereas the longer ones show unpredictable swishing. It is shown that the sensor is able to measure resistance changes due to deflections, but the wind tunnel tests did not show fluctuating behaviour or significant changes in standard deviation of the resistance data, as a result of high induced noise due to the wind. The cause for this is still unclear.

Looking back, the research question formulated for this research, as formulated in chapter 1, is:

To what extend is it possible to use the principle of a piezoresistive strain gauge in a 3D-printed sensor to measure the presence of stall over an airfoil in a qualitative way?

it can be concluded that a sensor has been successfully designed and fabricated. In general, the average resistance of this sensor was lower at stall, compared to laminar flow. The tuft is flapping as expected, as is showed in the video analysis and is thus able to measure stall. During tests, the fluctuations of the tuft could not be seen in the resistance data. However, it could when the flapping was induced manually by giving an initial force, indicating that the accuracy of the sensor itself or the measurement is not the problem.

Therefore, it can be concluded that the sensor is capable of measuring resistance changes due to a deflection, but that the presence of wind decreases the signal to noise ratio drastically. More research must be done into that, before deciding if this concept is a viable option for stall measurements. For that, recommendations are formulated in chapter 7.

A Nomenclature

List of variables:

A_c: cross-sectional area of sensor (m^2)
A_s: cross-sectional area of strain gauge (m^2)
AR: aspect ratio (-)
α: angle of attack (°)
b: width (m)
c: chord length (m)
Ca: Cauchy number (-)
e: distance between neutral axes of sensor and strain gauge (m)
F_s: sampling frequency (Hz)
GF: Gauge factor (-)
h: height (m)
I: current (A)
I_y: second moment of area in the y direction (m^4)
L: length (m)
R: resistance (Ω)
$\bar{R}$: average resistance (Ω)
Re: Reynolds number (-)
ρ: resistivity (Ωm)
ρ_f: density of fluid (kgm^{-3})
ρ_s: density of solid (kgm^{-3})
S: wing area (m^2)
$\mathcal{S}$: slenderness ratio (-)
σ: standard deviation (same unit as what it is the standard deviation of)
t: time (s)
Θ: bending angle (rad)
U: flow velocity (ms^{-1})
U_∞: free stream velocity (ms^{-1})
V_{in}: input voltage (V)
V_{out}: output voltage (V)

List of abbreviations:

AOA: angle of attack
FDM: fused deposition modeling
FFT: fast fourier transform
LEV: leading edge vortex
PSD: power spectral density
RaM: Robotics and Mechatronics

B Video analysis

(a) State 1: No movement

(b) State 2: 1D-flapping

(c) State 3: Swishing

(d) State 4: Reversed

Figure B.1: Snapshots of videos of the four states the aeroelastical behaviour can be in, as discussed in section 6.3

C Wind tunnel test results

Tests with first batch

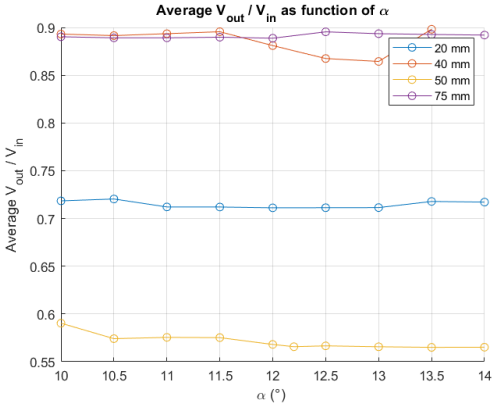

(a) Average $\frac{V_{\text{out}}}{V_{\text{in}}}$

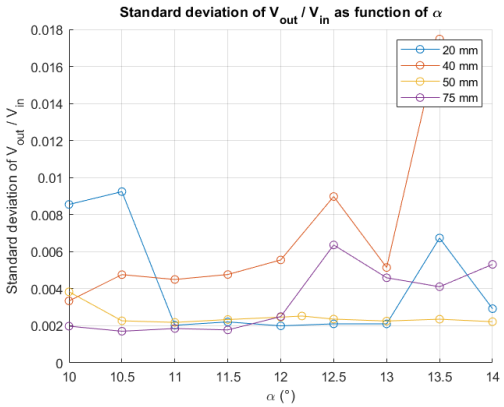

(b) Standard deviation

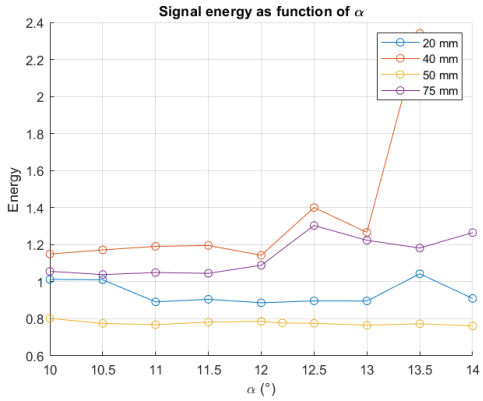

(c) Energy

Figure C.1: Average value, standard deviation and energy of $\frac{V_{\text{out}}}{V_{\text{in}}}$ measured for $U_\infty = 10\,\text{m}\,\text{s}^{-1}$

Bibliography

[1] "Clear flight solutions b.v." https://www.thedronebird.com/. Accessed: April 3, 2021.

[2] G. A. Folkertsma, W. Straatman, N. Nijenhuis, C. H. Venner, and S. Stramigioli, "Robird: A robotic bird of prey," *IEEE Robotics & Automation Magazine*, September 2017.

[3] "The portwings project." http://www.portwings.eu/. Accessed: March 31, 2021.

[4] W. Shyy, H. Aono, C.-K. Kang, and H. Liu, *An Introduction to Flapping Wing Aerodynamics*. Cambridge University Press, 2013.

[5] T. Y. Hubel and C. Tropea, "The importance of leading edge vortices under simplified flapping flight conditions at the size scale of birds," *Journal of Experimental Biology*, vol. 213, pp. 1930–1939, may 2010.

[6] J. C. Cui, "3d printed piezo-resistive flow sensors for use on wings," Master's thesis, University of Twente, March 2021.

[7] M. Schouten, G. Wolterink, A. Dijkshoorn, D. Kosmas, S. Stramigioli, and G. Krijnen, "A review of extrusion-based 3d printing for the fabrication of electro-and biomechanical sensors," *IEEE Sensors Journal*, 2020.

[8] J. Anderson, *Fundamentals of aerodynamics*. New York: McGraw-Hill, 1991.

[9] J. Anderson, *Introduction to flight*. New York: McGraw-Hill, 1989.

[10] H. Wagner, "Über die entstehung des dynamischen auftriebes von tragflügeln," *ZAMM - Zeitschrift für Angewandte Mathematik und Mechanik*, vol. 5, no. 1, pp. 17–35, 1925.

[11] S. P. Sane, "The aerodynamics of insect flight," *Journal of Experimental Biology*, vol. 206, pp. 4191–4208, dec 2003.

[12] J. Anders, "Biomimetic flow control," in *Fluids 2000 Conference and Exhibit*, American Institute of Aeronautics and Astronautics, jun 2000.

[13] T. Mitchel, S. Ramananarivo, and L. Ristroph, "Video: Color coding vortices to understand flapping wing propulsion," in *68th Annual Meeting of the APS Division of Fluid Dynamics - Gallery of Fluid Motion*, American Physical Society, nov 2015.

[14] M. A. Moelyadi, H. A. Putra, and G. Sachs, "Unsteady aerodynamics of flapping wing of a bird," *Journal of Engineering and Technological Sciences*, vol. 45, pp. 47–60, apr 2013.

[15] Cousera, "Fundamentals of fluid-solid interactions." https://www.coursera.org/learn/fluid-solid-interaction/home/welcome. Accessed: June 9, 2021.

[16] A. Dijkshoorn, P. Werkman, M. Welleweerd, G. Wolterink, B. Eijking, J. Delamare, R. Sanders, and G. J. M. Krijnen, "Embedded sensing: integrating sensors in 3-d printed structures," *Journal of Sensors and Sensor Systems*, vol. 7, pp. 169–181, mar 2018.

[17] F. Froes, *Additive manufacturing for the aerospace industry*. Amsterdam, Netherlands: Elsevier, 2019.

[18] G. Saggio, F. Riillo, L. Sbernini, and L. R. Quitadamo, "Resistive flex sensors: a survey," *Smart Materials and Structures*, vol. 25, p. 013001, dec 2015.

[19] K. T. Magar, A. M. Pankonien, G. W. Reich, and R. V. Beblo, "Aerodynamic parameter prediction via artificial hair sensors with signal power in turbulent flow," *AIAA Journal*, vol. 57, pp. 898–903, mar 2019.

[20] W. Su and G. W. Reich, "Artificial hair sensor designs for flow measurement of UAVs with different scales," in *Sensors and Smart Structures Technologies for Civil, Mechanical, and Aerospace Systems 2016* (J. P. Lynch, ed.), SPIE, apr 2016.

[21] B. T. Dickinson, *Detecting Fluid Flows with Bioinspired Hair Sensors*. PhD thesis, Oregon State University, 2009.

[22] S. Ristić, "Flow visualisation techniques in wind tunnels," *Scientific Technical Review, Vol.LVII, No.1*, 2007.

[23] L. Chen, T. Suzuki, T. Nonomura, and K. Asai, "Flow visualization and transient behavior analysis of luminescent mini-tufts after a backward-facing step," *Flow Measurement and Instrumentation*, vol. 71, p. 101657, mar 2020.

[24] N. Swytink-Binnema and D. A. Johnson, "Digital tuft analysis of stall on operational wind turbines," *Wind Energy*, vol. 19, pp. 703–715, may 2015.

[25] H. A. Service, "Airflow during a stall." https://www.youtube.com/watch?v=WFcW5-1NP60. Accessed: June 14, 2021.

[26] G. P. Corten, *Flow Separation on Wind Turbine Blades*. PhD thesis, Utrecht University, 2001.

[27] R. Roark, *Roark's formulas for stress and strain*. New York: McGraw-Hill, 2002.

[28] V. Koncar, *Smart Textiles for in Situ Monitoring of Composites*. San Diego: Elsevier Science & Technology, 2018.

[29] E. Hobert, "3d printed flexible fingertip strain sensor," June 2017. Bachelor's thesis, University of Twente.

[30] M. Al-Rubaiai, R. Tsuruta, U. Gandhi, C. Wang, and X. Tan, "A 3d-printed stretchable strain sensor for wind sensing," *Smart Materials and Structures*, vol. 28, p. 084001, jun 2019.

[31] D. Rosato and D. Rosato, "PRODUCT DESIGN," in *Plastics Engineered Product Design*, pp. 198–343, Elsevier, 2003.

[32] N. Anwar and F. A. Najam, "Understanding cross-sections," in *Structural Cross Sections*, pp. 39–136, Elsevier, 2017.

[33] J. Ochshorn, "Statics," in *Structural Elements for Architects and Builders*, pp. 1–37, Elsevier, 2010.

[34] E. de Langre, "Effects of wind on plants," *Annual Review of Fluid Mechanics*, vol. 40, pp. 141–168, jan 2008.

[35] "Rotary 3d printer + cnc mill | diabase engineering | united states." https://www.diabasemachines.com/hseries. Accessed: June 5, 2021.

[36] 3DHerndon, "Diabase h4 pro." https://3dherndon.com/diabase-engineering-5-axis-h-series-hybrid-3d-printer-and-cnc-mill.html. Accessed: June 23, 2021.

[37] "Ninjaflex 3d printer filament (85a)." https://ninjatek.com/shop/ninjaflex/. Accessed: June 1, 2021.

[38] "Palmiga innovation." https://palmiga.com/. Accessed: June 1, 2021.

[39] "Solidworks 2020: Improved performance." https://www.solidworks.com/media/solidworks-2020-improved-performance. Accessed: June 12, 2021.

[40] "Ultimaker cura." https://ultimaker.com/nl/software/ultimaker-cura. Accessed: June 5, 2021.

[41] Kapton, "1 mil kapton® tapes, rohs compliant." https://www.kaptontape.com/1_Mil_Kapton_Tapes.php. Accessed: June 19, 2021.

[42] Farnell, "1181 6mm tape, conductive shielding, copper foil, 6.35 mm x 16.5 m." https://nl.farnell.com/3m/1181-6mm/tape-copper-foil-16-5m-x-6mm/dp/1653451?st=Copper%20tape%203m. Accessed: June 19, 2021.

[43] Electrolube, "Silver conductive paint." https://electrolube.com/product/scpsilver-conductive-paint/. Accessed: June 15, 2021.

[44] E. B. Prakken, "3d printed flow sensor," Bachelor's thesis, University of Twente, February 2019.

[45] NXP, "Frdm-k64f: Freedom development platform for kinetis® k64, k63, and k24 mcus." https://www.nxp.com/design/development-boards/freedom-development-boards/mcu-boards/freedom-development-platform-for-kinetis-k64-k63-and-k24-mcus:FRDM-K64F. Accessed: June 12, 2021.

[46] ARM, "Mbed: Rapid iot device development." https://os.mbed.com/. Accessed: June 14, 2021.

[47] Wikipedia, "Voltage divider." https://en.wikipedia.org/wiki/Voltage_divider. Accessed: June 5, 2021.

[48] Wikipedia, "Wheatstone bridge." https://en.wikipedia.org/wiki/Wheatstone_bridge. Accessed: June 21, 2021.

[49] Aerolab, "Educational wind tunnel (ewt)." https://www.aerolab.com/aerolab-products/educational-wind-tunnel-ewt/. Accessed: June 21, 2021.

[50] Casio, "Ex-f1." http://arch.casio-intl.com/asia-mea/en/dc/ex_f1/. Accessed: June 15, 2021.

[51] Kinovea, "A microscope for your videos." https://www.kinovea.org/. Accessed: June 15, 2021.

[52] R. Meyers, *Encyclopedia of physical science and technology*. San Diego: Academic Press, 2002.

[53] Mathworks, "Lowpass-filter signals." https://nl.mathworks.com/help/signal/ref/lowpass.html#mw_3aa14271-5d7b-4a2a-8b29-b1f47d3ce414. Accessed: June 25, 2021.

[54] Fluke, "Productselector digitale multimeters." https://www.fluke.com/nl-nl/producten/elektrische-test-en-meetinstrumenten/digitale-multimeters. Accessed: June 22, 2021.

[55] J. Bae, J. Lee, S. Kim, J. Ha, B.-S. Lee, Y. Park, C. Choong, J.-B. Kim, Z. L. Wang, H.-Y. Kim, J.-J. Park, and U.-I. Chung, "Flutter-driven triboelectrification for harvesting wind energy," *Nature Communications*, vol. 5, sep 2014.

[56] M. Olsen, R. Zhang, J. Örtegren, H. Andersson, Y. Yang, and H. Olin, "Frequency and voltage response of a wind-driven fluttering triboelectric nanogenerator," *Scientific Reports*, vol. 9, apr 2019.